J. Fluid Mech. (2014), *vol.* 745, *pp.* 25–61.
doi:10.1017/jfm.2014.89

Spanwise-localized solutions of planar shear flows

J. F. Gibson† and E. Brand

Department of Mathematics and Statistics, University of New Hampshire, Durham, NH 03824, USA

(Received 22 April 2013; revised 6 January 2014; accepted 9 February 2014)

We present several new spanwise-localized equilibrium and travelling-wave solutions of plane Couette and channel flows. The solutions exhibit concentrated regions of vorticity that are centred over low-speed streaks and flanked on either side by high-speed streaks. For several travelling-wave solutions of channel flow, the vortex structures are concentrated near the walls and form particularly isolated and elemental versions of coherent structures in the near-wall region of shear flows. One travelling wave appears to be the invariant solution corresponding to a near-wall coherent structure educed from simulation data by Jeong *et al.* (*J. Fluid Mech.*, vol. 332, 1997, pp. 185–214) and analysed in terms of transient growth modes of streaky flow by Schoppa & Hussain (*J. Fluid Mech.*, vol. 453, 2002, pp. 57–108). The solutions are constructed by a variety of methods: application of windowing functions to previously known spatially periodic solutions, continuation from plane Couette to channel flow conditions, and from initial guesses obtained from turbulent simulation data. We show how the symmetries of localized solutions derive from the symmetries of their periodic counterparts, analyse the exponential decay of their tails, examine the scale separation and scaling of their streamwise Fourier modes, and show that they develop critical layers for large Reynolds numbers.

Key words: instability, nonlinear dynamical systems, transition to turbulence

1. Introduction

Over the last twenty years the computation of invariant solutions of the Navier–Stokes equations, or ‘exact coherent structures’, has opened a new approach to understanding the dynamics of moderate-Reynolds-number unsteady flows, an approach which promises to provide a long-hoped-for bridge between dynamical systems theory and turbulence. Unlike previous derivations of low-order dynamical models of unsteady flows (Lorenz 1963; Aubry *et al.* 1988; Holmes, Lumley & Berkooz 1996), the invariant-solutions approach forgoes low-d projections and simplified models and instead takes a well-resolved direct numerical simulation as a quantitatively accurate finite-dimensional approximation of the Navier–Stokes equations. The well-resolved simulation is then treated as a very high-dimensional dynamical system. The first step in analysis of a dynamical system is the computation of its invariant solutions: its equilibria, homo- and heteroclinic orbits, and periodic orbits. In the invariant-solutions view of turbulence, equilibrium solutions correspond

† Email address for correspondence: john.gibson@unh.edu

to steady states of the fluid flow, periodic orbits correspond to states of the fluid velocity field that repeat themselves exactly after a finite time, and homo- and heteroclinic orbits correspond to dynamic transitions between equilibria or periodic orbits. For flows with homogeneous spatial directions, such as pipes and channels, continuous symmetries in the equations of motion allow relative invariant solutions, e.g. travelling waves (relative equilibria) and relative periodic orbits.

The simplest invariant solutions of fluids are the classical, closed-form steady states of the Navier–Stokes equations, for example, the parabolic laminar flow profile of pressure-driven channel and pipe flow, or the linear laminar solution of plane Couette flow. Solutions such as these have special cancellations which make it possible to represent the exact solution of the nonlinear system with a finite set of simple functions. For example, for the laminar solution of channel flow, the nonlinear term vanishes and the solution can be represented exactly as a second-order polynomial in the wall-normal variable. However, if we consider the problem from the perspective of faithful, very high-dimensional finite discretizations, invariant solutions are the solutions of nonlinear algebraic or differential equations in 10^4 or more free variables. Only a few very special solutions (the classical ones) will involve few enough modes to be expressible in closed form, and most will involve nonlinear coupling between large numbers of non-zero variables. Compared to the classical closed-form solutions, these computed invariant solutions are typically unstable, fully three-dimensional, fully nonlinear, distant from the smooth laminar flow solutions, and involve most if not all of the available modes of the numerical representation. Determination and specification of such solutions is necessarily numerical.

The practical feasibility of finding such high-dimensional nonlinear solutions of the Navier–Stokes equations was first demonstrated by Nagata (1990), who computed an unstable three-dimensional nonlinear equilibrium solution of plane Couette flow at a Reynolds number above the onset of turbulence, using a 589-dimensional discretization. The same equilibrium solution was found independently and analysed in greater precision and detail by Clever & Busse (1992) and Waleffe (1998, 2003). A large number of equilibria and travelling waves of plane Couette and pipe flow have since been found (Nagata 1997; Schmiegel 1999; Faisst & Eckhardt 2003; Wedin & Kerswell 2004; Gibson, Halcrow & Cvitanović 2009), a few of channel flow (Itano & Toh 2001; Waleffe 2001), and in other flows such as square duct flow (Wedin, Bottaro & Nagata 2009; Okino *et al.* 2010; Uhlmann, Kawahara & Pinelli 2010). Periodic orbits have been calculated for plane Couette flow (Kawahara & Kida 2001; Viswanath 2007; Cvitanović & Gibson 2010; Willis, Cvitanović & Avila 2013) pipe flow (Duguet, Pringle & Kerswell 2008), and two-dimensional Kolmogorov turbulence (Chandler & Kerswell 2013), and hetero- and homoclinic connections for plane Couette flow (Gibson, Halcrow & Cvitanović 2008; Halcrow *et al.* 2009; van Veen & Kawahara 2011). Improved numerical methods and more powerful computers now allow the computation of solutions with as many as 10^6 free variables. High-resolution calculations have shown that discretization errors converge toward zero as resolution is increased, demonstrating that the numerical solutions are precise approximations of true solutions of the continuous Navier–Stokes equations, rather than artifacts of discretization. High-resolution calculations have also allowed accurate computation of solutions with fine spatial structure, such as periodic orbits that exhibit turbulent ‘bursting’ phases (Viswanath 2007; Cvitanović & Gibson 2010).

Just as in low-dimensional dynamical systems theory, the importance of these invariant solutions stems from the organization they impose on the state-space dynamics. In particular, dynamics in the neighbourhood of (relative) equilibria

and periodic orbits is governed to leading order by the linearization about these solutions, and the eigenvalues of the linearized dynamics reveal the local character of the state-space flow and the dimensionality of each solution's unstable manifold. For shear flows at moderate Reynolds numbers and in closed or small periodic domains, most known invariant solutions have a positive but remarkably small number of unstable eigenvalues, and correspondingly low-dimensional unstable manifolds. For example, the equilibrium solution of plane Couette flow developed by Nagata, Busse, Clever, and Waleffe (hereafter termed the NBCW equilibrium) has a single unstable eigenvalue (Wang, Gibson & Waleffe 2007), and the periodic orbit solutions of Viswanath (2007) have between one and 11 unstable eigenvalues. This low dimensionality of instability is a crucially important result. It suggests, as long suspected, that moderate-Reynolds-number flows are inherently low-dimensional, at least for small confined domains. It further suggests that the temporal dynamics of such flows results from a relatively low-dimensional, chaotic but deterministic walk between the flow's unstable invariant solutions, along the low-dimensional network of their unstable manifolds (Gibson *et al.* 2008). Moreover, the coherent structures often observed in such flows can be understood as resulting from close passes to these unstable invariant solutions, on which the Navier–Stokes equations balance exactly. Waleffe's term 'exact coherent structures' expresses this idea well (Waleffe 2001), and from here on we use that term and 'invariant solutions' interchangeably. Indeed, a key feature of the NBCW invariant solution is that it captures structure commonly observed in shear flows in the form of wavy rolls that support alternating streaks of high and low streamwise velocity (see § 2.2 for further discussion). We refer the reader to the Kawahara, Uhlmann & van Veen (2012) review article for an excellent overview of research in this area.

Most of the development of the invariant-solutions approach has been done in the context of minimal flow units (Jiménez & Moin 1991; Hamilton, Kim & Waleffe 1995); that is, small, periodic domains just large enough to sustain turbulent flow or contain a single coherent structure. For example, most of the above-cited work on plane Couette flow is for doubly-periodic boxes with stream- and spanwise periodic lengths just a few multiples of the wall separation; in pipe flow solutions are typically computed with periodic boundary conditions in the axial direction, with periodic length between one and five pipe diameters. Minimal flow units are a reasonable simplifying assumption in the study of exact coherent structures, since they reproduce key features and statistics of moderate-Reynolds-number turbulence on extended domains with fewer degrees of freedom. Invariant solutions, particularly periodic orbits, have been shown to quite accurately capture the spatial structures and temporal dynamics of minimal flow units. On the other hand, there are differences between minimal and extended turbulence, and invariant solutions computed in minimal flow units will be necessarily biased towards the former. For example, the Jiménez *et al.* (2005) comparison of the solutions of minimal flows to extended turbulence found rough agreement in the length scales of the solutions with comparable length scales in extended turbulence, but that velocity fluctuations of the Kawahara & Kida (2001) unstable periodic orbits in minimal flows were substantially smaller than those observed locally in extended flows, and that while minimal flows at low Reynolds number visited these solutions at least occasionally, such visitations were rare for turbulence in extended domains.

Minimal flow units also rule out consideration of structure at large length scales, which is known to play an important role in transition. For example, in moderate-Reynolds-number pipe flow, turbulence first appears in streamwise-localized

transient puffs (Hof *et al.* 2006) and proliferates to sustained turbulence when the spreading of the puffs outpaces their decay (Avila *et al.* 2011). Similarly, in spatially extended plane Couette flow at moderate Reynolds numbers, localized perturbations trigger turbulent spots that then invade the surrounding laminar flow (Lundbladh & Johansson 1991; Daviaud, Hegseth & Berge 1992; Tillmark & Alfredsson 1992), sometimes exhibiting long-wavelength patterns of turbulent stripes (Barkley & Tuckerman 2005).

The assumption of minimal flow units also complicates coordination of theory and experiment, since small periodic cells are not experimentally realizable. Close passes to unstable travelling waves with axial periodicity have been detected in experimental pipe flows (Hof *et al.* 2004; de Lozar *et al.* 2012), but the effort to match experiment and theory would be greatly aided if invariant solutions could be computed for boundary conditions that can be achieved in experiment, for example, as localized perturbations within otherwise laminar flow. More broadly, it seems to us that a fundamental motivation for research in coherent structures is the idea that certain localized flow configurations undergo relatively autonomous evolution, for example, that a packet of hairpin vortices undergoes a pattern of evolution determined largely by the packet's internal organization and comparatively weakly influenced by the surrounding flow. This view is implicit in studies that compute coherent structures through conditional averages (Adrian 2007 and references therein), since finite correlation lengths then naturally produce localized structures, and it is consistent with the Robinson (1991) definition of a coherent structure as 'a three-dimensional region of the flow over which at least one fundamental variable ... exhibits significant correlation with itself over a range of space and/or time that is significantly larger than the smallest local scales of the flow'. Thus we are motivated to find spatially localized Navier–Stokes solutions for several reasons: to demonstrate that invariant solutions are not computational artifacts that occur only for idealized conditions of minimal flow units, to facilitate actuation and detection of invariant solutions in experiment, and to provide a basis for addressing both large-length-scale structure and localized coherent structure in extended flows.

Several papers have made valuable contributions in the computation of spatially localized solutions of canonical shear flows. The first instance of localization was found in the spanwise direction alone, in the Schneider, Marinc & Eckhardt (2010*b*) computation of spanwise-localized equilibrium and travelling waves of the Navier–Stokes equations, via an 'edge-tracking' algorithm for plane Couette flow in a streamwise-periodic but spanwise-extended domain. These solutions are spanwise-localized forms of the spatially-periodic NBCW solution which exhibit exponential decay towards laminar flow in the spanwise coordinate. Schneider, Gibson & Burke (2010*a*) demonstrated a number of interesting connections between the localized solutions of Schneider *et al.* (2010*b*) and localized solutions of the Swift–Hohenberg equation. Both systems exhibit homoclinic snaking, a process by which localized solutions grow additional structure at their fronts via a sequence of saddle–node bifurcations in a continuation parameter (see § 4.2 for further discussion). This is an intriguing connection, as Swift–Hohenberg is a key model equation in the theory of pattern formation (Hoyle 2006), for which localization is comparatively well-understood (Burke & Knobloch 2007). More recently, Avila *et al.* (2013) found a streamwise-localized travelling wave of pipe flow that closely resembles the transient turbulent puffs of Hof *et al.* (2006). Since the remaining (azimuthal) homogeneous direction in pipe flow is naturally periodic, the streamwise-localized Avila *et al.* (2013) solution is experimentally realizable in a way that the singly-localized solutions of

plane Couette flow are not. The solution of Avila *et al.* (2013) is strong evidence that localized puffs and spots are in fact intimately connected to localized invariant solutions.

Deguchi, Hall & Walton (2013) generated localized forms of the EQ7/HVS solution of plane Couette flow (Gibson *et al.* 2009; Itano & Generalis 2009) via computations on a reduced system obtained from asymptotic analysis in the limit of high Reynolds number Re and small streamwise wavenumber $\alpha \sim 1/Re$. In particular they find that EQ7/HVS localizes in the spanwise direction as the spanwise wavenumber γ decreases. This spanwise-localized solution appears to correspond to the spanwise-localized EQ7-1 solution computed for the full Navier–Stokes equations at finite Reynolds number in § 2.5 of this paper, and we have verified that the periodic EQ7/HVS solution localizes in the spanwise direction at moderate Reynolds numbers ($Re = 400$) under continuation to small γ. The evidence for streamwise localization for small α in Deguchi *et al.* (2013) seems less convincing. Our numerical simulations at finite but large Re in the appropriate range of α replicated the velocity fields of Deguchi *et al.* (2013), but, consistent with their figure 14(*a*), displayed only small variations in amplitude over the streamwise coordinate, as opposed to convergence towards laminar flow.

Some time-varying fluid states with both spanwise and streamwise localization have been found. Schneider *et al.* (2010*b*) found a chaotically wandering state of plane Couette flow with exponential localization in both span- and streamwise directions. A similar time-varying doubly-localized state was found by Duguet, Schlatter & Henningson (2009), with several quasi-steady minima. Cherubini *et al.* (2011) computed a slowly-developing edge state of streamwise-developing Blasius flow that is localized in the wall-normal and streamwise directions and periodic in the spanwise. Visualizations of this edge state in Q-criterion isosurfaces are very similar to those of hairpin vortices in Adrian (2007). It should be noted that each of these doubly-localized, time-varying edge states undergoes an irregular and non-repeating evolution in time. These states are thus not invariant solutions of the given flows, but they do suggest the existence of doubly-localized solutions nearby.

The specific results and organization of this paper are as follows. In § 2 we construct several spanwise-localized solutions of plane Couette flow by a windowing and refinement method that, unlike edge-tracking, puts no restrictions on the number of the solution's unstable eigenmodes. We show how the symmetries of localized solutions result from the symmetries and phase of the underlying periodic solution. In § 3, to further develop the invariant-solutions approach in experimentally accessible flow conditions, we construct localized travelling-wave solutions of channel flow, by windowing and refining periodic solutions obtained by continuation from plane Couette conditions and by searching among turbulent simulation data. In doing so we find particularly intriguing travelling-wave solutions of channel flow whose vorticity is concentrated in the near-wall region, in spanwise and wall-normal localized structures that closely resemble structures educed from numerical simulation data by Jeong *et al.* (1997) analysed in terms of transient growth modes of streaky flow by Schoppa & Hussain (2002). In § 4 we analyse the tails of the localized solutions and show that they decay exponentially to laminar flow at the rate determined solely by the streamwise wavenumber of the solution, with far-field structure that is independent of the details of the core region. We examine scale separation and scaling in the streamwise Fourier harmonics and development of critical layers at large Reynolds numbers.

2. Equilibrium solutions of plane Couette flow

2.1. *Governing equations and numerical methods*

Plane Couette flow consists of an incompressible fluid confined between two parallel rigid plates moving in-plane at a constant relative velocity. The $\boldsymbol{x} = (x,\ y,\ z)$ coordinates are aligned with the streamwise, wall-normal and spanwise directions, where streamwise is defined as the direction of relative wall motion. We assume a computational flow domain $\Omega = [-L_x/2,\ L_x/2] \times [-h,\ h] \times [-L_z/2,\ L_z/2]$ with periodic boundary conditions in x and z and no-slip conditions at the walls $y = \pm h$. We restrict our attention to streamwise-periodic velocity fields and L_x chosen to match the streamwise wavelength. In the spanwise direction, we choose L_z either to match the spanwise wavelength of a spanwise-periodic field, or to a large value that approximates a spanwise-infinite domain. We decompose the total velocity and pressure fields into sums of a laminar base flow and a deviation from laminar: $\boldsymbol{u}_{tot}(\boldsymbol{x},\ t) = \boldsymbol{u}(\boldsymbol{x},\ t) + U(y)\,\boldsymbol{e}_x$ and $p_{tot} = p(\boldsymbol{x},\ t) + x\ \mathrm{d}P/\mathrm{d}x$, where $\mathrm{d}P/\mathrm{d}x$ is a fixed constant specifying an imposed mean pressure gradient. For plane Couette flow we will consider only the case $\mathrm{d}P/\mathrm{d}x = 0$, for which the laminar solution is $U(y) = \bar{U}y/h$, where $\bar{U}$ is half the relative wall speed. After non-dimensionalization by $\bar{U}$, h, and the kinematic viscosity ν, the Navier–Stokes equations for plane Couette flow can be written

$$\frac{\partial \boldsymbol{u}}{\partial t} + U\frac{\partial \boldsymbol{u}}{\partial x} + v\ U'\,\boldsymbol{e}_x + \boldsymbol{u}\cdot\boldsymbol{\nabla}\boldsymbol{u} = -\boldsymbol{\nabla}p + \frac{1}{Re}\nabla^2\boldsymbol{u}, \qquad \boldsymbol{\nabla}\cdot\boldsymbol{u} = 0, \tag{2.1}$$

where $Re = \bar{U}h/\nu$ and the velocity components are $\boldsymbol{u}(\boldsymbol{x},\ t) = [u,\ v,\ w](x,\ y,\ z,\ t)$. In this decomposition the plane Couette laminar solution is $U(y) = y$, $\mathrm{d}P/\mathrm{d}x = 0$, $\boldsymbol{u} = 0$, and $p = 0$. From here on we refer to $\boldsymbol{u}$ as velocity and $\boldsymbol{u}_{tot}$ as total velocity, and we note that $\boldsymbol{u}$ has zero Dirichlet boundary conditions at the walls.

We express the symmetries of plane Couette and channel flows in terms of symmetries

$$\left.\begin{aligned} \sigma_x &: [u,\ v,\ w](x,\ y,\ z) \to [-u,\ v,\ w](-x,\ y,\ z),\\ \sigma_y &: [u,\ v,\ w](x,\ y,\ z) \to [u,\ -v,\ w](x,\ -y,\ z),\\ \sigma_z &: [u,\ v,\ w](x,\ y,\ z) \to [u,\ v,\ -w](x,\ y,\ -z),\\ \tau(\Delta x,\ \Delta z) &: [u,\ v,\ w](x,\ y,\ z) \to [u,\ v,\ w](x+\Delta x,\ y,\ z+\Delta z). \end{aligned}\right\} \tag{2.2}$$

For $(\ell_x,\ \ell_z)$-periodic fields we define two discrete, half-box translation operators

$$\tau_x = \tau(\ell_x/2,\ 0), \qquad \tau_z = \tau(0,\ \ell_z/2) \tag{2.3}$$

and we express products of these symmetries by concatenation of subscripts, e.g. $\sigma_{xy} = \sigma_x\sigma_y : [u,\ v,\ w](x,\ y,\ z) \to [-u,\ -v,\ w](-x,\ -y,\ z)$ and $\tau_{xz} = \tau_x\tau_z = \tau(\ell_x/2,\ \ell_z/2)$. Note that these definitions differ from (3.1), (3.4) and (3.5) of Gibson *et al.* (2009), in order to accommodate channel as well as plane Couette conditions and to treat the exponents on τ_x and τ_z more conventionally. We use the standard group-theory notation $\langle \ldots \rangle$ to indicate the group generated by a set of group elements; e.g. $\langle \sigma_{xy},\ \sigma_z \rangle = \{e,\ \sigma_{xy},\ \sigma_z,\ \sigma_{xyz}\}$ where e is the identity.

The Navier–Stokes equations (2.1) with plane Couette conditions and y-Dirichlet, x, z-periodic boundary conditions are invariant under any combination of rotation by π about the z axis, reflection about the $z = 0$ plane, and finite translations in the x and z directions. The symmetry group of plane Couette flow is thus $\langle \sigma_{xy},\ \sigma_z,\ \tau(\Delta x,\ \Delta z) \rangle$.

For each subgroup of this group, there is a subspace of velocity fields that is invariant under the equations of motion. That is, if a velocity field $\boldsymbol{u}(\boldsymbol{x}, 0)$ satisfies $\boldsymbol{u} = \sigma\boldsymbol{u}$ for each symmetry σ in a given subgroup, $\boldsymbol{u}(\boldsymbol{x}, t)$ will satisfy the same symmetries for all time. Invariant solutions of the equations of motion naturally lie in these subspaces. For example, with appropriate choice of the origin, equilibrium solutions of plane Couette flow typically have either σ_{xyz} or both σ_{xy} and σ_z symmetry, since these require the velocity field to vanish at the origin, and so prevent drifting in x and z.

Equilibrium solutions of plane Couette flow are computed using the Newton–Krylov-hookstep search algorithm of Viswanath (2007, 2009) to solve the equation $\boldsymbol{f}^T(\boldsymbol{u}) - \boldsymbol{u} = 0$, where $\boldsymbol{f}^t : \boldsymbol{u}(0) \to \boldsymbol{u}(t)$ is the finite-time integration of (2.1) with appropriate boundary conditions. Time integration is performed with a Fourier–Chebyshev-tau scheme in primitive variables (Spalart, Moser & Rogers 1991; Canuto *et al.* 2006) and third-order semi-implicit backwards differentiation time stepping (Peyret 2002). Spatial discretization levels are specified by the $N_x \times N_y \times N_z$ grid used for collocation calculation of nonlinear terms with 2/3-style dealiasing. We set spatial discretization levels so that the maximum truncated Fourier and Chebyshev modes are $O(10^{-6})$ and $O(10^{-10})$ respectively. Coarser discretization for the present problems sometimes produces spurious solutions. Symmetries are enforced through the search by projecting $\boldsymbol{u} \to (\boldsymbol{u} + \sigma\boldsymbol{u})/2$ for each of the generators σ of the appropriate symmetry group at the intervals $\Delta T = 1$ during time integration. The residual of the discretized search equation is $\|\boldsymbol{f}^T(\boldsymbol{u}) - \boldsymbol{u}\|/T$, using the L^2 norm

$$\|\boldsymbol{u}\| = \left[\frac{1}{V}\int_V \boldsymbol{u}\cdot\boldsymbol{u}\,\mathrm{d}\boldsymbol{x}\right]^{1/2}, \tag{2.4}$$

where V is the volume of the computational domain. The search algorithm typically solves the discretized equations to a residual of $O(10^{-14})$; that is, the spectral coefficients of $\boldsymbol{f}^T(\boldsymbol{u})$ and $\boldsymbol{u}$ are equal to nearly double precision. The accuracy of a given discretized solution as an approximate solution to the continuous equations is estimated by increasing its spatial resolution by a factor of 3/2 in each direction, decreasing the time step by a factor of two, and then recomputing the residual at the higher resolution. Solutions are typically accurate to $O(10^{-6})$, consistent with the size of the truncated spectral coefficients. Further details of the implementation of the search algorithm and time integration are given in Gibson *et al.* (2009), and the code is available for download at www.channelflow.org (Gibson 2013).

2.2. *Spatially periodic solutions: EQ1/NBCW, EQ7/HVS, and EQ8*

Figure 1 shows a visualization of three spatially periodic equilibrium solutions of plane Couette flow: the well-known 'lower branch' solution of Nagata (1990), Clever & Busse (1992) and Waleffe (1998) (NBCW, called EQ1 in Gibson *et al.* 2009), and the 'hairpin vortex solution (HVS)' of Itano & Generalis (2009) and discovered independently as EQ7 in Gibson *et al.* (2009). Henceforth we refer to these as NBCW and EQ7. EQ8 is the upper branch of the EQ7 solution. The NBCW solution is well-known not only as the first known exact nonlinear solution to the Navier–Stokes equations, but also for a number of remarkable characteristics, which we outline briefly here. The NBCW solution captures precisely, in the context of plane Couette flow, the roll–streak structure that seems ubiquitous in shear flows ranging from Taylor–Couette to the turbulent boundary layer, and consequently forms an example of an exact instantaneous balance between the three cycles of Waleffe's

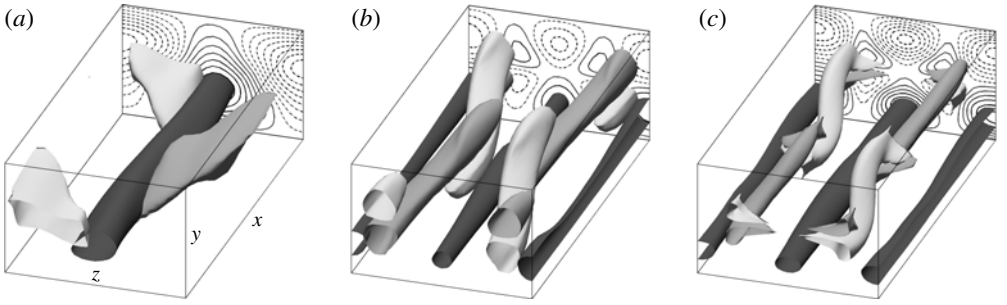

FIGURE 1. Three spatially periodic equilibria of plane Couette flow. (*a*) NBCW lower branch, (*b*) EQ7 lower branch, and (*c*) EQ8 (upper branch of EQ7), all at $Re = 400$ and $\alpha, \gamma = 1, 2$, where α and γ are the streamwise and spanwise wavenumbers. The visualizations show three-dimensional isosurfaces of signed swirling strength at (*a*,*b*) $s = \pm 0.09$ and (*c*) $s = \pm 0.2$ in light/medium grey (see text). Isosurfaces of streamwise velocity indicating high-speed streaks are shown in dark grey at (*a*) $u = 0.4$, (*b*) $u = 0.15$, and (*c*) $u = 0.3$. The back plane shows contours of streamwise velocity at levels $u = \pm\{0.03, 0.09, 0.15, \ldots, 0.45\}$ with dashed/solid lines indicating negative/positive values. Note that by symmetry both solutions have streaks of equal magnitude and opposite streamwise velocity; these are not shown in the isosurfaces to reduce clutter, but they are indicated by the negative/positive symmetry of the back-plane contours of streamwise velocity. The origin is at the centre of the box.

self-sustaining process for shear flows (Waleffe 1997, 1998). The NBCW solution has also served as a starting point for recent efforts to formulate a dynamical-systems theory of turbulence. At Reynolds numbers above the onset of turbulence, the NBCW solution lies between the laminar solution and the chaotic turbulent region of state space. It has a single unstable eigenvalue across a wide range of Reynolds numbers, if only fundamental and superharmonic perturbations are allowed (Wang *et al.* 2007), so that its stable manifold forms a boundary between states that decay to laminar flow and states that grow to turbulence (Schneider *et al.* 2008). The comparatively low viscous shear rate of the NBCW solution suggests that it might be feasible to implement a control strategy to stabilize this single unstable direction and obtain savings in the wall driving force compared to the turbulent flow (Kawahara 2005; Wang *et al.* 2007). The NBCW solution also has been shown to have well-defined asymptotic structure in the limit of large Reynolds number, which can be exploited to form a reduced system that accurately captures the structure of the solution over a wide range of Reynolds numbers (Wang *et al.* 2007; Hall & Sherwin 2010). The asymptotic structure and reduced system are particularly relevant for this work, since it seems likely that any analytic understanding of localization in Navier–Stokes solutions will be more easily developed in the context of a reduced system.

The EQ7 solution has been conjectured to be related to hairpin vortices frequently observed in the turbulent boundary layer (Itano & Generalis 2009). However it should be noted that the hairpin shapes shown in the visualizations of Itano & Generalis (2009) are vortex lines, whereas hairpin vortices are typically illustrated using criteria that highlight the magnitude of vortices, such as the Q criterion, lambda criterion, or swirling strength (Adrian 2007). Figure 1 shows NBCW, EQ7, and EQ8 visualized with signed swirling strength isosurfaces to show the roll structure and streamwise velocity isosurfaces to show high-speed streaks. Neither EQ7 nor EQ8 appear to have hairpin structure in this plot, nor do they when visualized with the Q or lambda

criterion. The swirling strength at $\boldsymbol{x}$ is defined as the magnitude of the complex part of the eigenvalue of the velocity gradient tensor $\boldsymbol{\nabla u}(\boldsymbol{x})$ (Zhou *et al.* 1999). We chose swirling strength over other measures of fluid circulation such as the Q criterion because it most clearly identified in three-dimensional isosurfaces the regions of highly concentrated circulation that are apparent in two-dimensional quiver plots such figure 5. Since the invariant solutions in this paper have elongated regions of concentrated circulation nearly aligned with the x axis, we attached a $\pm$ sign to the swirling strength that indicates clockwise/counterclockwise circulation with respect to the positive x axis, following Wu & Christensen (2006) and Stanislas, Perret & Foucaut (2008).

2.3. *Construction of localized initial guesses by spanwise windowing*

The localized equilibria and travelling waves of plane Couette flow described in Schneider *et al.* (2010*b*) and Schneider *et al.* (2010*a*) are spanwise-localized versions of the spatially-periodic NBCW solution. These localized solutions are comprised of a core region that closely resembles the periodic NBCW solution, weak tails that decay exponentially towards laminar flow, and a transitional region between the core and tails. This form suggests that new localized solutions might be found by imposing a similar core-transition-tail structure on other known spatially periodic solutions, and then refining these initial guesses with a Newton–Krylov solver. The rough form of this desired structure can be imposed on initial guesses by multiplying a known spatially-periodic solution, expressed as a perturbation on laminar flow, by an even positive windowing function $W(z)$ that is nearly unity over a core region $|z| < a$, decreases smoothly and monotonically to nearly zero over a transition region $a \leqslant |z| < a + b$, and vanishes as $|z| \to \infty$, followed by projecting the resulting field $W(z)\boldsymbol{u}(\boldsymbol{x})$ onto the divergence-free subspace. We have found that with a robust Newton–Krylov solver, the precise details of the windowing function and the projection are unimportant, and that the only important details are smoothness and the widths of the core and transition regions. One choice that suffices is the windowing function

$$W(z) = \frac{1}{4}\left(1 + \tanh\left(\frac{6(a-z)}{b} + 3\right)\right)\left(1 + \tanh\left(\frac{6(a+z)}{b} + 3\right)\right). \tag{2.5}$$

This $W(z)$ behaves as desired: it is even, smooth, monotonic in $|z|$, satisfies $0.995 < W(z) < 1$ for $|z| < a$ and $0 < W(z) < 0.005$ for $|z| > a + b$, and it approaches zero exponentially as $|z| \to \infty$. Here $W(z)$ is specified in this particular form because we found that the most important factor in producing a good initial guess was the size and location of the transition region, which are specified by the parameters a and b. A sufficient projection is to apply $W(z)$ to the streamwise and spanwise components of velocity and reconstruct the wall-normal from the divergence-free condition. That is, let $\boldsymbol{u} = [u, v, w]$ be a z-periodic solution expressed as a perturbation over laminar flow. An initial guess for a z-localized solution $\boldsymbol{u}_g = [u_g, v_g, w_g]$ can be constructed by setting $u_g = Wu$, $w_g = Ww$, and reconstructing v_g from $\boldsymbol{\nabla} \cdot \boldsymbol{u}_g = 0$ and boundary conditions. This projection has the advantage of being localized in x and z; that is, $v_g(x, y, z)$ is determined by a differential equation in y in which x and z appear only parametrically, and that requires v_g to vanish along with u_g and w_g for large $|z|$. Note that $\boldsymbol{\nabla} \cdot (W(z)\,\boldsymbol{u}(\boldsymbol{x})) = W'(z)\,w(\boldsymbol{x})$ for incompressible $\boldsymbol{u}$; therefore one can minimize the corrections for incompressibility by choosing the transition region, where $W'(z)$ is large, to coincide with spanwise bands where w is on average small. We also

tested satisfying incompressibility by applying the windowing function to the vertical velocity–vorticity representation and inverting; initial guesses produced in this way had much weaker z-localization but sometimes resulted in the same solution under a Newton–Krylov-hookstep search.

It is worth emphasizing that the localization procedure is rather crude. By construction, the initial guess should be close to equilibrium in the core region and the tails – nearly but not exactly because the guess merely approaches the laminar solution for large z, and because the non-local effect of pressure will corrupt the balance of terms that one would otherwise expect in the core region where $W(z)$ is very nearly unity. In the transition region, however, there is no reason to expect that the velocity field that smoothly interpolates between tails and core will be close to equilibrium. The quality of these initial guesses, thus, depends entirely on the robustness of the solver used to refine the initial guess into a solution. In particular, within the transition region the initial guess is too far from equilibrium to be refined to an exact solution with a straight Newton method and requires instead a so-called globally convergent search algorithm such as the hookstep (Dennis & Schnabel 1996; Viswanath 2007, 2009).

2.4. *Localization and symmetry*

The symmetries of a desired solution are important both in determining solution type (e.g. equilibrium versus travelling wave) and for reducing the search space, which improves the speed and robustness of the search. The appropriate symmetries for spanwise-localized solutions are determined as follows. We begin with a spanwise-periodic solution with a known set of symmetries. Multiplying that solution by a non-periodic windowing function $W(z)$ breaks any of these symmetries that involve z periodicity. Symmetries that do not involve z periodicity are preserved through the localization procedure and form the symmetry group of the localized guess. Note further that the symmetry group G of a periodic solution $\boldsymbol{u}$ transforms by conjugation to $\tau G \tau^{-1}$ when the solution is phase-shifted to $\tau\boldsymbol{u}$, and that the localization procedure will break and preserve the different symmetry groups of $\boldsymbol{u}$ and $\tau\boldsymbol{u}$ differently. Thus it is possible to construct localized guesses with different symmetry groups by applying the windowing function to the same periodic solution in different spatial phases.

To illustrate, we show how the symmetries of the equilibrium, travelling wave, and rung solutions of plane Couette flow in Schneider *et al.* (2010*a*) arise from localizing the NBCW solution in different spatial phases. In the spatial phase of Waleffe (2003), the (ℓ_x, ℓ_z)-periodic NBCW solutions have symmetry group $\langle \tau_x\sigma_z, \tau_z\sigma_{xyz}\rangle = \{e, \tau_x\sigma_z, \tau_{xz}\sigma_{xy}, \tau_z\sigma_{xyz}\}$, which is the S symmetry group of Gibson *et al.* (2009). (Note that in Gibson *et al.* 2009, the y subscript on σ_{xy} was suppressed.) The localizing procedure above sets $[u_g, w_g](x, y, z) = W(z)[u, w](x, y, z)$ and determines v_g from incompressibility. A simple series of substitutions shows that the first symmetry is preserved under localization, $\boldsymbol{u}_g = \tau_x\sigma_z\boldsymbol{u}_g$, but the second and third symmetries are not: $\boldsymbol{u}_g \neq \tau_{xz}\sigma_{xy}\boldsymbol{u}_g$ and $\boldsymbol{u}_g \neq \tau_z\sigma_{xyz}\boldsymbol{u}_g$. Intuitively, since the windowing function $W(z)$ is constant in x and y and even about $z = 0$ but not periodic in z, windowing preserves the z-reflection, x-translation symmetry $\tau_x\sigma_z$ of the NBCW solution, but not its $\tau_{xz}\sigma_{xy}$ or $\tau_z\sigma_{xyz}$ symmetries, which both involve z periodicity. The sole preserved symmetry, $\tau_x\sigma_z$, is in fact the symmetry of the localized travelling wave reported in Schneider *et al.* (2010*a*), i.e. $[u_g, v_g, w_g](x, y, z) = [u_g, v_g, -w_g](x + \ell_x/2, y, -z)$. Refinement of this initial guess by a search method that respects symmetry results in a travelling-wave solution with the same symmetries.

The same localization process on a shifted NBCW solution produces an initial guess with the symmetry of the localized equilibrium solutions of Schneider *et al.* (2010*a*). Shifting the NBCW solution by a quarter-wavelength in z, i.e. by $\tau_z^{1/2} = \tau(0, \ell_z/4)$, thus changes its symmetry group by conjugation $\tau_z^{1/2} s \tau_z^{-1/2}$ from $\{e, \tau_x\sigma_z, \tau_{xz}\sigma_{xy}, \tau_z\sigma_{xyz}\}$ to $\{e, \tau_{xz}\sigma_z, \tau_{xz}\sigma_{xy}, \sigma_{xyz}\} = \langle \tau_{xz}\sigma_z, \sigma_{xyz}\rangle$ which is the R_{xz} symmetry group of Gibson *et al.* (2009). Of these symmetries, the z-localization breaks $\tau_{xz}\sigma_z$ and $\tau_{xz}\sigma_{xy}$, since they involve periodicity in z, and leaves only σ_{xyz} symmetry, which is in fact the symmetry of the localized equilibrium of plane Couette flow reported in Schneider *et al.* (2010*a*). For choices of z phase that are not integer multiples of $\ell_z/4$, each of the three symmetries of the periodic solution is broken by the localization, leaving completely unsymmetric initial guesses, corresponding to the rung solutions of Schneider *et al.* (2010*a*).

2.5. *Spanwise-localized equilibria of plane Couette flow: computation*

In this section we construct new spanwise-localized equilibrium solutions of plane Couette flow by applying windowing and refinement to the spatially periodic EQ7 solution. Figure 2 illustrates how spanwise-localized initial guesses with different symmetry groups are constructed from different spatial phases of the spatially periodic solution. Figure 2(*a*) shows EQ7 at $Re = 400$ with fundamental streamwise and spanwise wavenumbers $\alpha, \gamma = 1, 2$ (i.e. periodic lengths $\ell_x = 2\pi/\alpha = 2\pi$ and $\ell_z = 2\pi/\gamma = \pi$). The figure shows three copies of the periodic structure in the $z \in [3\pi/2,\ 3\pi/2]$ subset of the full $L_x, L_z = 2\pi, 6\pi$ computational domain. The spatial phase of EQ7 in figure 2(*a*) is chosen so that one concentrated vortex structure is centred on the $z = 0$ plane. In this phase the solution has symmetry group $\langle \sigma_{xy}, \tau_{xz}, \tau_x\sigma_z\rangle$. Each of these symmetries is readily apparent in the figure, keeping in mind that the orientation of swirling with respect to the x axis and thus the shade of the isosurfaces changes under σ_{xy} (rotation about z axis) and $\tau_x\sigma_z$ (x-shift, z-reflect symmetry). The windowing function $W(z)$ is plotted as a function of z on the front face of the box. Multiplication of the periodic structure shown in figure 2(*a*) by the windowing function, followed by projection onto the divergence-free subspace as described in § 2.3, produces the initial guess shown in figure 2(*c*). In this case the windowing parameters $a, b = 0.3, 1$ were chosen to preserve the single concentrated vortex structure centred on the $z = 0$ plane and to taper rapidly to nearly zero before the next vortical structure. The w component of EQ7 drops from $O(10^{-1})$ to $O(10^{-2})$ between the concentrated vortices, so placing the transition region of the windowing function in this region also minimizes corrections on the initial guess for incompressibility, as discussed in § 2.3. The localization in z breaks the τ_{xz} symmetry of the periodic solution, since it involves z periodicity, leaving a localized initial guess with symmetry group $\langle \sigma_{xy}, \tau_x\sigma_z\rangle$. Any solution in this symmetry group will be an equilibrium, since the x reflection in σ_{xy} prevents travelling waves in x and the z reflection in $\tau_x\sigma_z$ symmetry prevents travelling waves in z.

Figure 2(*b*,*d*) illustrates construction of a localized initial guess with different symmetries by windowing the periodic solution in a different spanwise phase. Figure 2(*b*) shows the same periodic EQ7 solution as in figure 2(*a*), but translated by a quarter-wavelength in z. In this phase the periodic NBCW solution has symmetries $\langle \sigma_{xy}, \sigma_z, \tau_{xz}\rangle$, which are again readily apparent in the figure (and which can be derived by conjugating $\langle \sigma_{xy}, \tau_{xz}, \tau_x\sigma_z\rangle$ with quarter-wavelength shift $\tau_z^{1/2}$ and choosing the specified symmetries as generators for the conjugated group). A wider windowing function, with $a = b = 1$, preserved a pair of mirror-symmetric concentrated vortical

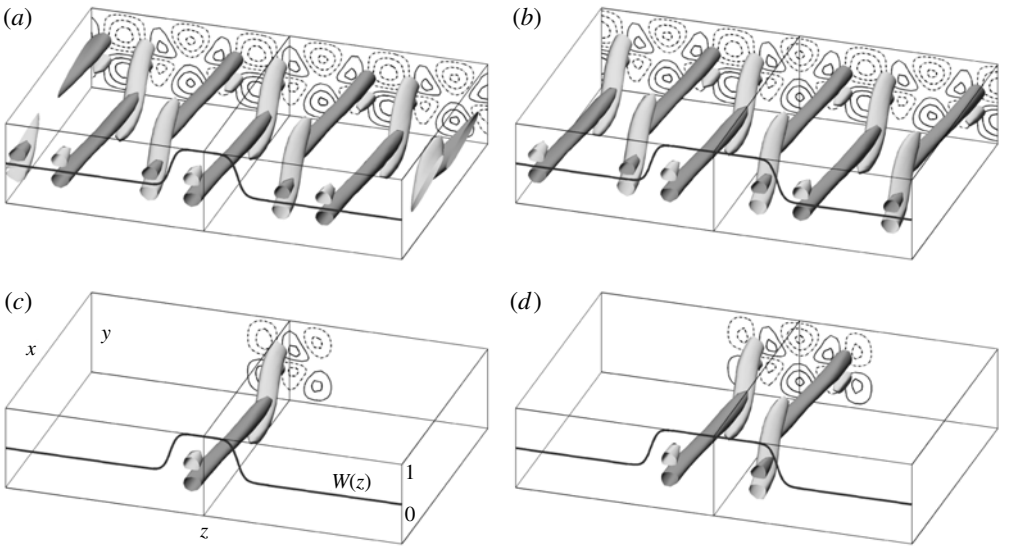

FIGURE 2. Construction of localized initial guesses by windowing. (*a*,*b*) The spatially periodic EQ7 solution of plane Couette flow, in two spatial phases. Three copies of the α, $\gamma = 1, 2$ periodic solution at $Re = 400$ are shown in the $z \in [-3\pi/2,\ 3\pi/2]$ subset of the full L_x, $L_z = 2\pi, 6\pi$ computational domain, with the $z = 0$ plane shown bisecting the box to highlight the z symmetries. The solutions in (*a*) and (*b*) are related by a quarter-wavelength phase shift in z. (*c*,*d*) Initial guesses for localized solutions with different symmetry groups, produced by multiplying (*a*,*b*) by windowing functions $W(z)$ (heavy line on front planes). Isosurfaces of signed swirling strength at $s = \pm 0.12$ are shown in (light/medium grey) and contours of streamwise velocity on the back plane at contour levels $u = \pm\{0.03, 0.09, 0.15\}$.

structures in the core region and tapered rapidly to nearly zero before reaching the next vortices, as shown in figure 2(*b*). The windowing breaks symmetries with factors of τ_{xz}, producing an initial guess for a spanwise-localized solution with symmetry group $\langle \sigma_{xy}, \sigma_z \rangle$. Again, sign changes in all three coordinates in this symmetry group fix the phase of the velocity field with respect to the origin and rule out travelling waves. Thus, the localized solutions in both choices of z phase will be equilibria, unlike the localized solutions of Schneider *et al.* (2010*a*), where one choice of phase produces equilibria and the other streamwise-travelling waves.

The localized initial guesses depicted in figure 2(*c*,*d*) were then refined to numerically exact equilibrium solutions of plane Couette flow shown in figure 3(*a*,*c*) using methods discussed in § 2.1. These solutions were computed at $Re = 400$ in a $2\pi, 6\pi$ computational box and a $32 \times 65 \times 192$ grid, with integration time $T = 10$ and time step $\mathrm{d}t = 0.0625$, resulting in a CFL number of ~ 0.7 The residuals $\|\boldsymbol{f}^T(\boldsymbol{u}) - \boldsymbol{u}\|/T$ of the discretized equations began at roughly 10^{-3} for the windowed initial guesses and were reduced to $O(10^{-14})$ after six or seven iterations of the Newton–Krylov-hookstep algorithm. The discretized solutions were found to approximate solutions of the continuous equations to $O(10^{-6})$, as discussed in § 2.1. The tails of the localized solutions drop to $O(10^{-4})$ at the $z = \pm 3\pi$ edge of the computational domain. The computational cost is modest: about one CPU-hour for each solution, running serially on a desktop computer with a 3.3 GHz Intel i7-3960X processor.

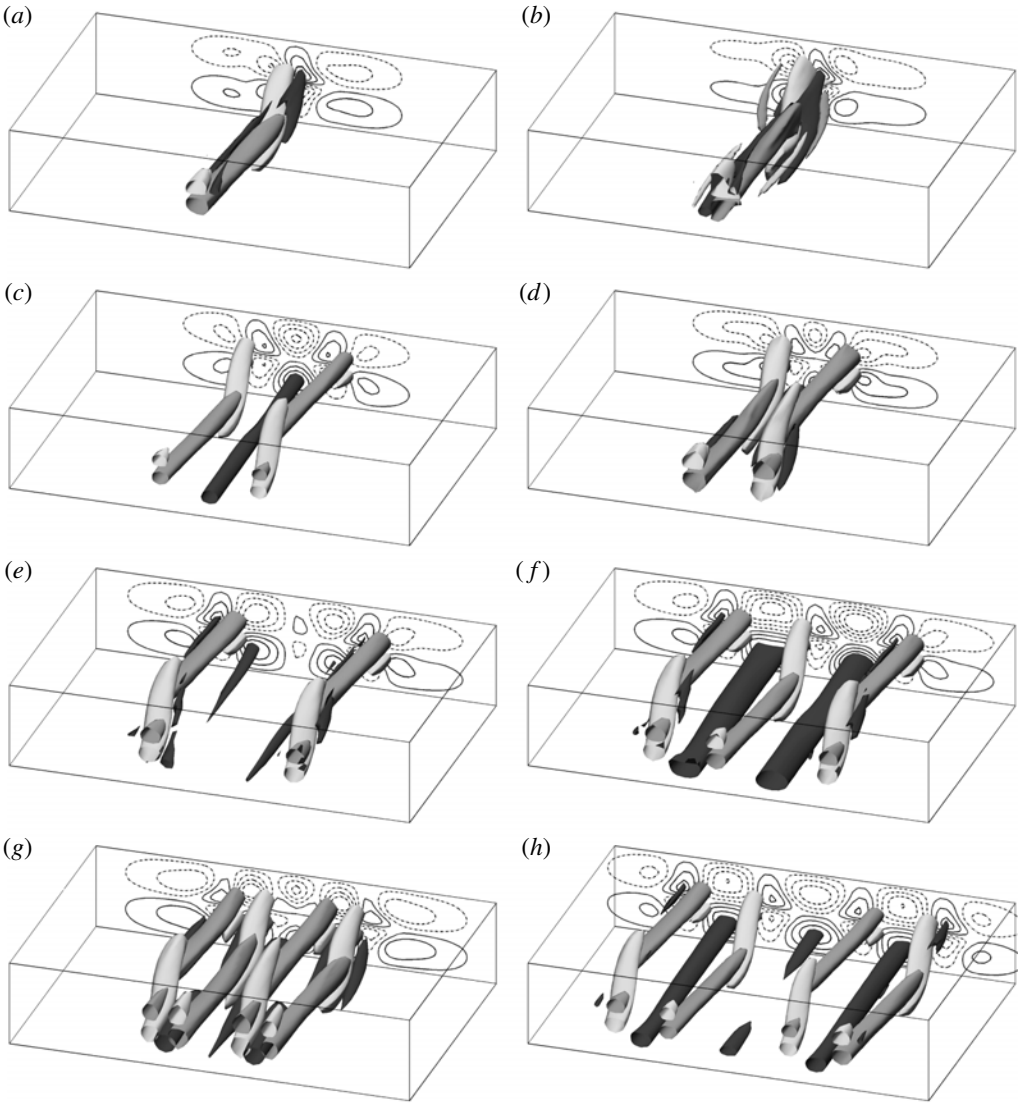

FIGURE 3. Spanwise-localized equilibrium solutions of plane Couette flow at $Re = 400$: (*a*) and (*b*) the lower and upper branches of EQ7-1, respectively, (*c*,*d*) those of EQ7-2, (*e*,*f*) EQ7-3, and (*g*,*h*) EQ7-4. The plotting conventions are the same as in figure 2 with swirling strength isosurfaces at $s = \pm 0.14$, but additional isosurfaces of streamwise velocity at $u = 0.2$ are plotted in dark grey to show the positions of high-speed streaks near the lower wall. Symmetric high-speed streaks near the upper wall are not shown. The $z \in [-3\pi/2, 3\pi/2]$ subset of the $L_x, L_z = 2\pi, 6\pi$ computational domain is shown.

2.6. *Spanwise-localized equilibria of plane Couette flow: properties*

Figure 3 shows four spanwise-localized equilibrium solutions of plane Couette flow with streamwise wavenumber $\alpha = 1$ and $Re = 400$. The four rows show distinct solutions EQ7-1,2,3,4 with 1,2,3,4 copies of the basic concentrated vortical structure shown in isolation in figure 3(*a*), with the lower branch of each solution on the left and the upper branch on the right. EQ7-1,3 have $\langle \sigma_{xy}, \tau_x \sigma_z \rangle$ symmetry and EQ7-2,4

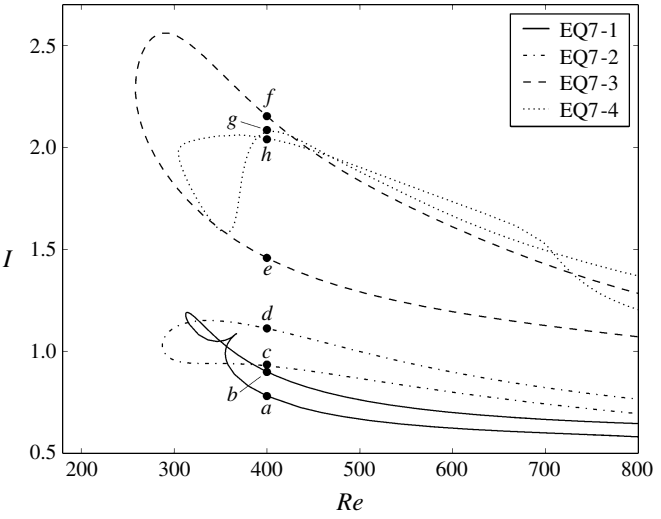

FIGURE 4. Bifurcation diagram of localized solutions of plane Couette flow. Integrated shear rate I as defined in (2.6) versus Re for localized equilibria of plane Couette flow. Labelled points correspond to solutions depicted in figure 3(*a–h*).

have $\langle \sigma_{xy}, \sigma_z \rangle$ symmetry. Figure 3(*a*,*c*,*f*,*h*) were obtained by the localization and search methods outlined in § 2.5, (*a*,*c*) from the initial guesses shown in figure 2(*c*,*d*), and (*f*,*h*) by increasing the core region of the window to fit three and four copies of the concentrated vortex structures. The opposite branches (*b*,*d*,*e*,*g*) were obtained by continuation in Reynolds number.

Figure 4 shows a bifurcation diagram of the EQ7-1,2,3,4 solutions under continuation in Reynolds number. The vertical axis is the integrated shear rate I defined as

$$I = \frac{1}{2L_x} \int_{-L_x/2}^{L_x/2} \int_{-L_z/2}^{L_z/2} \left(\left. \frac{\partial u}{\partial y} \right|_{y=1} + \left. \frac{\partial u}{\partial y} \right|_{y=-1} \right) \mathrm{d}x \, \mathrm{d}z. \tag{2.6}$$

Note that this measure of shear is not normalized by L_z, in order to make I insensitive to the choice of computational domain for spanwise-localized solutions. Since the deviation $\boldsymbol{u}$ from laminar flow of a localized solution vanishes exponentially at large z, the integral on the right-hand side of (2.6) approaches a finite constant as $L_z \to \infty$, making I as defined insensitive to L_z for large L_z. Note that each of the EQ7-1,2,3,4 solutions lies on a distinct solution branch. This is in contrast to the localized versions of the NBCW solutions, for which all solutions with the same symmetry lie on a single solution branch, and additional copies of the fundamental structure grow at the fronts in a continuous fashion along the solution branch while the internal structure remains constant.

Following convention we designate the lower versus upper branches of the EQ7-1,2,3,4 solutions based on the shear rate of the two branches immediately after each saddle–node bifurcation. However, the lower versus upper branch designation provides a less natural classification scheme for these solutions than it does for spatially periodic solutions. Broadly characterized, the lower branches of spatially periodic solutions are closer to laminar flow and the upper branches are closer to turbulence by a number of measures, including shear rate, energy norm, instability,

		Symmetry	α, γ	Re	L_x, L_z	Grid	Accur.	Tails	Pos. λ_r	Max λ_r
NBCW		$\langle \tau_x\sigma_z, \tau_z\sigma_{xyz} \rangle$	1, 2	400	$2\pi, \pi$	$20 \times 49 \times 36$	10^{-7}	–	1	0.047
NBCW		$\langle \tau_x\sigma_z, \tau_z\sigma_{xyz} \rangle$	1, 2	400	$2\pi, 6\pi$	$20 \times 49 \times 216$	10^{-7}	–	5	0.047
EQ7		$\langle \sigma_{xy}, \tau_{xz}, \tau_x\sigma_z \rangle$	1, 2	400	$2\pi, \pi$	$24 \times 65 \times 36$	10^{-8}	–	3	0.070
EQ7		$\langle \sigma_{xy}, \tau_{xz}, \tau_x\sigma_z \rangle$	1, 2	400	$2\pi, 6\pi$	$24 \times 65 \times 216$	10^{-8}	–	21	0.070
EQ7-1	LB	$\langle \sigma_{xy}, \tau_x\sigma_z \rangle$	1, –	400	$2\pi, 6\pi$	$32 \times 65 \times 192$	10^{-6}	10^{-5}	4	0.047
EQ7-1	UB	$\langle \sigma_{xy}, \tau_x\sigma_z \rangle$	1, –	400	$2\pi, 6\pi$	$40 \times 65 \times 216$	10^{-6}	10^{-5}	9	0.111
EQ7-2	LB	$\langle \sigma_{xy}, \sigma_z \rangle$	1, –	400	$2\pi, 6\pi$	$24 \times 65 \times 162$	10^{-6}	10^{-4}	6	0.066
EQ7-2	UB	$\langle \sigma_{xy}, \sigma_z \rangle$	1, –	400	$2\pi, 6\pi$	$32 \times 65 \times 192$	10^{-6}	10^{-4}	7	0.045
EQ7-3	LB	$\langle \sigma_{xy}, \tau_x\sigma_z \rangle$	1, –	400	$2\pi, 6\pi$	$32 \times 65 \times 192$	10^{-7}	10^{-4}	12	0.058
EQ7-3	UB	$\langle \sigma_{xy}, \tau_x\sigma_z \rangle$	1, –	400	$2\pi, 6\pi$	$32 \times 65 \times 162$	10^{-7}	10^{-4}	11	0.054
EQ7-4	LB	$\langle \sigma_{xy}, \sigma_z \rangle$	1, –	400	$2\pi, 6\pi$	$32 \times 65 \times 192$	10^{-7}	10^{-4}	15	0.048
EQ7-4	UB	$\langle \sigma_{xy}, \sigma_z \rangle$	1, –	400	$2\pi, 6\pi$	$24 \times 65 \times 162$	10^{-6}	10^{-4}	13	0.064

TABLE 1. Characteristics of equilibrium solutions of plane Couette flow. The last two columns show the number of eigenvalues with positive real part and the maximum real part respectively. Accuracy and tails are as described in § 2.1. LB and UB denote lower and upper branch respectively.

and smoothness (Gibson *et al.* 2009). The same holds true for the lower and upper branches of EQ7-1,2, but not for EQ7-3,4, whose upper branches are smoother and less unstable than their lower branches (see table 1). Judging by the visualizations in figure 3, the sequence of one, two, three, and four copies of the same unit of concentrated vortical structure is formed by EQ7-1 lower, EQ7-2 lower, EQ7-3 upper, and EQ7-4 upper, and in fact for EQ7-3 and EQ7-4, windowing and refinement produced the upper branches rather than the lower. Additionally, for EQ7-4, the lower branch most closely resembles the upper branch of EQ7-2.

The spatial structure of the EQ7-1 and EQ7-2 lower branches is illustrated in more detail in figure 5. Figure 5(*a–e*) shows the cross-stream velocity $[v, w](yz)$ for the lower branch of EQ7-1 in five streamwise-normal cross-sections spaced evenly between $x = -\pi$ and $x = 0$, which are the front face and the middle of the box in figure 3(*a*). The medium grey isosurface of signed swirling strength in the front half of the box in figure 3(*a*) appears here as a concentrated counter-clockwise vortex that begins just below and to the left of the origin at $x = -\pi$ in figure 5(*a*), increases in strength and moves upward and to the right in (*b–d*), and ends above and to the right of the origin at $x = 0$ in (*e*). By the $\tau_x\sigma_z$ symmetry of EQ7-1, the equivalent quiver plots for $x = 0$ to $x = \pi$ would be the z-mirror images of (*a–e*), showing a concentrated clockwise vortex starting below and to the right of the origin and moving upwards and leftwards, and corresponding to the light grey isosurface of signed swirling strength in the back half of the box in figure 3(*a*). Likewise, the predominant features of EQ7-2 shown in figure 5(*f–j*) are two z-symmetric counter-rotating vortices that begin near the lower wall at $x = -\pi$ in (*f*), and rise upwards and closer together in (*g–j*). Due to the σ_{xy} symmetry of EQ7-2, cross-sections from $x = 0$ to π would appear as the y-mirror images of (*j–f*), with a pair of nearby counter-rotating vortices in the lower half of the (y, z) plane rising and separating, as in the back half of figure 3(*c*). The clear and distinct concentrations of circulating fluid in figure 5 constitute our main justification for speaking of 'regions of concentrated vortical structure' and show that isosurface plots of signed swirling strength are not misleading but rather show precisely where such regions lie.

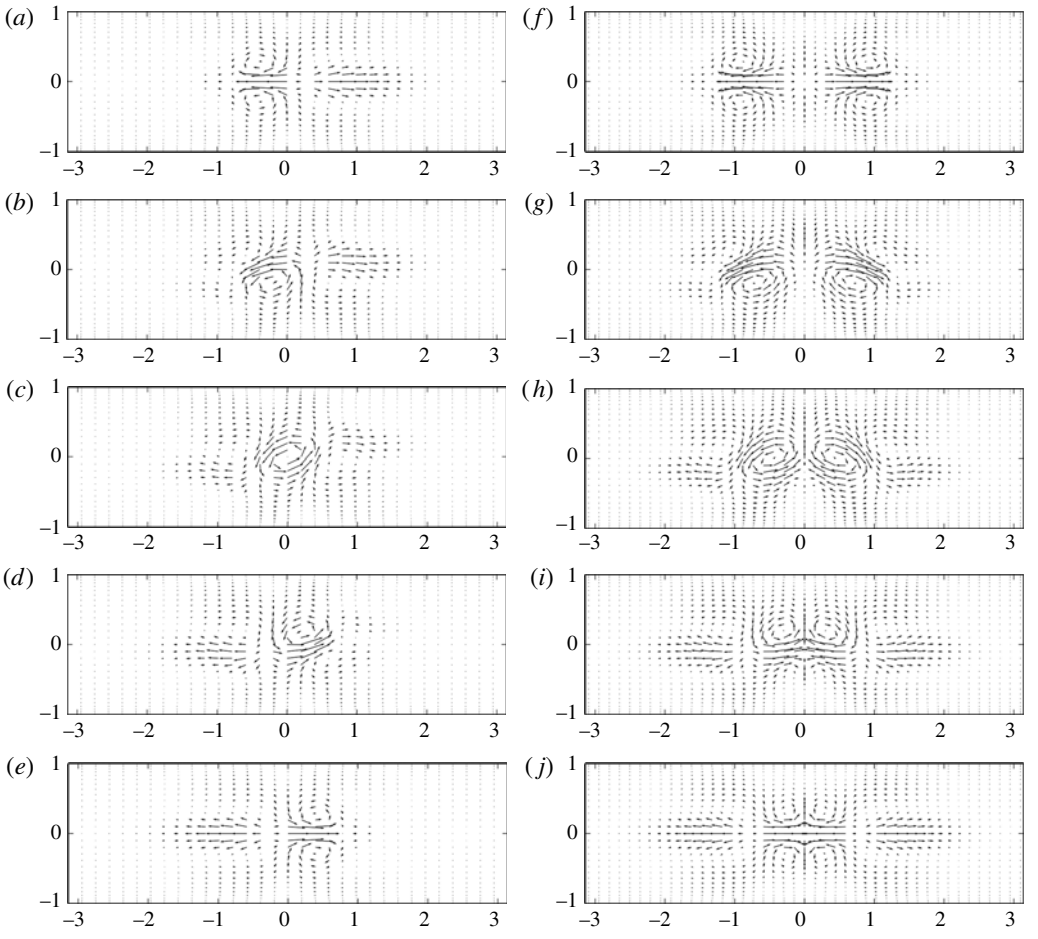

FIGURE 5. Cross-sections of spanwise-localized equilibrium solutions of plane Couette flow. (*a–e*) Quiver plots of $[v, w](y, z)$ for EQ7-1 lower branch at $x = \{-\pi, -3\pi/4, -\pi/2, -\pi/4, 0\}$ with y vertical and z horizontal. (*f–j*) EQ7-2 lower branch at the same x values. Here $\alpha = 1$ and $Re = 400$ for all plots. Compare to the same solutions shown with isosurfaces of signed swirling strength in figure 3(*a*,*c*); the cross-sections here are evenly spaced along the front half of those figures. The $z \in [-\pi, \pi]$ subset of the full $z \in [-3\pi, 3\pi]$ computational domain is shown.

The mean roll–streak structure of EQ7-1 and EQ7-2 is illustrated in figure 6. The four counter-rotating vortices surrounding the origin in figure 6(*a*) result from x-averaging the counter-clockwise vortex that slopes upwards and rightwards from $x = -\pi$ to 0 in figure 3(*a*) and figure 5(*a–e*) with its clockwise $\tau_x\sigma_z$-symmetric counterpart that slopes upwards and leftwards from $x = 0$ to π. These four vortices create the pattern of alternating positive and negative streamwise streaks (relative to laminar flow) shown in figure 6(*b*) by advecting high-speed fluid ($u_{tot} = \pm 1$) from the walls towards the interior in the region near $z = 0$, and low-speed fluid ($u_{tot} \approx 0$) from the interior towards the walls for larger z. Figure 6(*c*,*d*) shows the corresponding mean roll–streak structure for EQ7-2; here the doubling of the basic concentrated vortex structure compared to EQ7-1, apparent in figure 3(*c*), results in

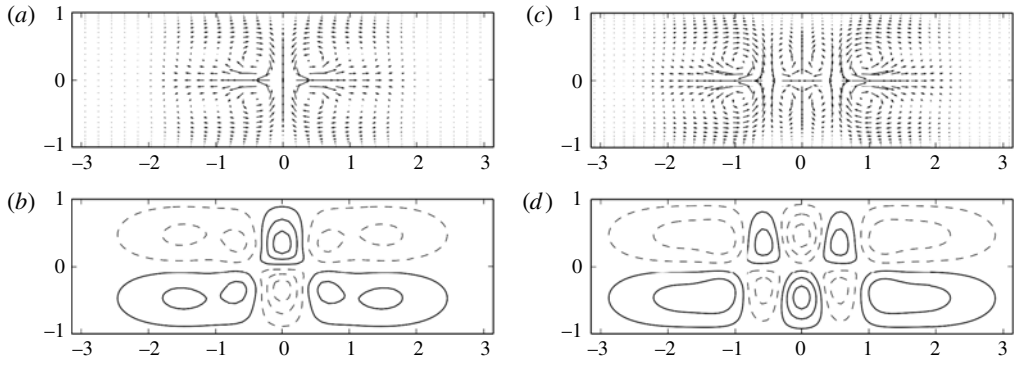

FIGURE 6. Streamwise-averaged roll–streak structure of spanwise-localized equilibria of plane Couette flow. (*a*) Quiver plot of x-average $[v, w](y, z)$ and (*b*) contour plot of x-average $u(y, z)$ for EQ7-1 lower branch with y vertical and z horizontal. (*c*,*d*) The same, but for EQ7-2 lower branch. Both solutions are shown at $\alpha = 1$ and $Re = 400$. Contour lines are plotted at levels $u = \pm\{0.03, 0.09, 0.15\}$, with negative values in dashed lines and positive in solid. Quiver plots are autoscaled. The $z \in [-\pi, \pi]$ subset of the full $z \in [-3\pi, 3\pi]$ computational domain is shown.

the eight counter-rotating mean vortices shown in figure 6(*c*) and an increased pattern of alternating streamwise streaks shown in figure 6(*d*).

Table 1 summarizes physical characteristics and discretization properties of the EQ7-1,2,3,4 solutions in comparison to the periodic NBCW and EQ7 solutions. The NBCW solution has a single unstable eigenvalue in its fundamental domain $L_x, L_z = \ell_x, \ell_z = 2\pi/\alpha, 2\pi/\gamma = 2\pi, \pi$, but additional subharmonic instabilities appear when the eigenvalue calculation is performed in domains that hold several copies of the periodic structure. The additional four spanwise subharmonic instabilities for NBCW at $L_x, L_z = 2\pi, 6\pi$ consist of two additional real eigenvalues, each of which appears twice, corresponding to eigenfunctions at two different phases in z. Similar calculations revealed additional streamwise subharmonic instabilities for NBCW, and similar considerations apply for EQ7. The numbers of unstable eigenvalues for EQ7-1,2,3,4 are comparable to the instability of NBCW when subharmonics compatible with the $L_x, L_z = 2\pi, 6\pi$ domain are included. We are not aware of previous calculations of subharmonic instabilities for the NBCW solution. The existence of subharmonic instabilities means that NBCW is more unstable as a repeated pattern in an extended domain than as a single structure in a minimal flow unit. This is consistent with the observation of Jiménez *et al.* (2005) that such states are visited less frequently in extended flows, and it suggests that stabilizing an experimental flow about the NBCW solution would require a higher-dimensional control strategy than suggested by the eigenvalue analysis in the minimal flow unit.

3. Travelling-wave solutions of channel flow

In this section we extend the results of § 2 to Poiseuille (channel) flow conditions. For the first set of solutions, we use a numerical continuation method similar in spirit to Waleffe's homotopy of the NBCW solution between plane Couette and 'half-Poiseuille' flow with no-slip at the lower wall and free-slip conditions at the upper wall (Waleffe 1998, 2001). When extended by symmetry to full channel conditions, Waleffe's continuation produces a travelling-wave solution symmetric about

the channel midplane, with two NBCW-like roll–streak structures, each positioned in the high-shear region near each wall, and mirror symmetric (σ_y) to each other across the midplane.

In the present study, we continue the EQ7 solutions from plane Couette to full channel conditions, enforcing no-slip boundary conditions on both walls throughout. The continuation is done in two stages: first with fixed wall speed and increasing pressure gradient, then fixed pressure gradient and decreasing wall speed. As in § 2.1, we decompose the total velocity field into a base flow and a deviation, $\boldsymbol{u}_{tot}(\boldsymbol{x}, t) = \boldsymbol{u}(\boldsymbol{x}, t) + U(y)\,\boldsymbol{e}_x$, and the total pressure field into $p_{tot} = p(\boldsymbol{x}, t) + x\,\mathrm{d}P/\mathrm{d}x$, where $\mathrm{d}P/\mathrm{d}x$ is a parametric constant corresponding to the externally imposed mean pressure gradient. To make the decomposition unique, we specify that the fluctuation pressure p is periodic (so that the spatial mean of $\boldsymbol{\nabla} p$ is zero), and that the base flow $U(y)$ satisfies the no-slip conditions at the walls and balances the imposed mean pressure gradient, $\mathrm{d}P/\mathrm{d}x = \nu U''$, where ν is the kinematic viscosity of the fluid. Consequently the base flow is the laminar solution for the given flow conditions and the fluctuation velocity satisfies zero Dirichlet conditions at the walls.

The Navier–Stokes equations again take the form of (2.1). The Reynolds number $Re = \bar{U}h/\nu$ is based on a velocity scale $\bar{U}$ appropriate to the flow as it transforms from plane Couette to pressure-driven Poiseuille conditions, namely, $\bar{U}$ is half the relative wall speed when continuing in pressure gradient and the centreline velocity of the laminar base flow when continuing in wall speed ($\bar{U} = |\mathrm{d}P/\mathrm{d}x|\,h^2/(2\nu)$). Thus in non-dimensional terms the continuation is first in mean pressure gradient $\mathrm{d}P/\mathrm{d}x$ from 0 to $-2/Re$ with wall speeds fixed at $U(\pm 1) = \pm 1$ (equivalently from $U(y) = y$ to $U(y) = 1 + y - y^2$), and then continuation in wall speed from 1 to 0 with mean pressure gradient held fixed at $P_x = -2/Re$ (equivalently from $U(y) = 1 + y - y^2$ to $U(y) = 1 - y^2$). For channel flow conditions $U(y) = 1 - y^2$ and $\mathrm{d}P/\mathrm{d}x \neq 0$, (2.1) and boundary conditions are invariant under any combination of x and z translations and reflections about the $y = 0$ and $z = 0$ midplanes; thus the symmetry group of channel flow is $\langle \sigma_y,\ \sigma_z,\ \tau(\Delta x, \Delta z)\rangle$. Travelling waves are computed as solutions of $\boldsymbol{f}^T(\boldsymbol{u}) - \tau(c_x T, 0)\boldsymbol{u} = 0$, where $\boldsymbol{f}^t$ is the finite-time integration of (2.1) and $\tau(c_x t, 0)$ is a streamwise shift of length $c_x t$ with the wave speed c_x a free parameter.

3.1. *Spatially periodic travelling-wave solutions of channel flow*

TW1: Figures 7(*a*) and 8(*a*,*b*) show a spatially periodic travelling-wave solution of channel flow with symmetry $\langle \sigma_y, \sigma_z, \tau_{xz}\rangle$ obtained by continuation from plane Couette conditions, as described above. The starting point for continuation was the spatially periodic EQ7 equilibrium of plane Couette flow at $Re = 2000$ and $\alpha,\ \gamma = 1, 2$; the TW1 channel travelling wave has the same spatial periodicity and is shown at $Re = 2300$. Note that TW1 is mirror symmetric about the $y = 0$ midplane. The y mirror symmetry is most clearly seen in the streamwise-averaged plots of cross-stream and streamwise velocity in figure 8(*a*,*b*). Although σ_y symmetry is within the symmetry group of channel flow, we did not expect the continuation to produce a solution with this symmetry, since it was neither present in the initial plane Couette solutions nor allowed in the intermediate steps in the continuation from plane Couette to channel conditions. Instead, we expected that the increasing y asymmetry under continuation in pressure gradient would push the vortex structures towards the lower wall, where the shear of the base flow is higher ($|U'(-1)| = 3$, compared to $|U'(1)| = 1$, for the base flow $U(y) = 1 + y - y^2$ attained at the end of the pressure continuation), and that this y asymmetry would be maintained during continuation in wall speed down

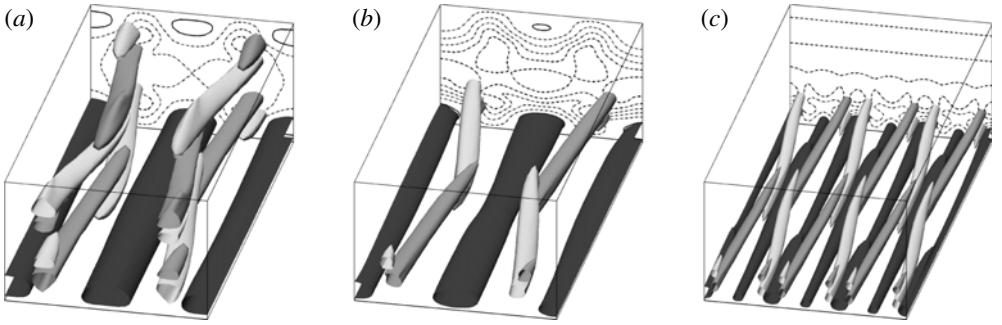

FIGURE 7. Spatially periodic travelling waves of channel flow with decreasing wall-normal symmetry. (*a*) TW1, constructed by continuing EQ7 from plane Couette to channel conditions, has symmetry group $\langle\sigma_y, \sigma_z, \tau_{xz}\rangle$. Isosurfaces of signed swirling strength at $s = \pm 0.04$ are shown in light/medium grey. High-speed streaks near the lower wall are shown by dark grey isosurfaces of streamwise velocity at $u = 0.02$. High-speed streaks near the upper wall, symmetric to those near the lower wall, are not shown as isosurfaces but they are indicated in the contour plots of streamwise velocity on the back plane. (*b*) TW2, found from an initial guess judiciously chosen from numerical simulation data, has symmetry group $\langle\sigma_z, \tau_{xz}\rangle$. Isosurfaces of signed swirling strength at $s = \pm 0.10$ are shown in light/medium grey, and high-speed streaks near the lower wall are shown by dark grey isosurfaces of streamwise velocity at $u = 0.03$. There are similar but weaker vortex structures and high-speed streaks near the upper wall, but they do not appear at these levels for the isosurfaces. Both (*a*) and (*b*) are shown at $\alpha, \gamma = 1, 2$ and $Re = 2300$. (*c*) TW3, constructed by continuation in Reynolds number from TW2 and further symmetrization and Newton–Krylov refinement, has $\langle\sigma_z, \tau_{xz}\rangle$ but periodicity $\alpha, \gamma = 1, 6$, and is shown at $Re = 4000$. Isosurfaces of signed swirling strength are at $s = \pm 0.9$ and $u = 0.03$. Each back plane shows a contour plot of streamwise velocity at levels $u = \{0.03, -0.03, -0.09, -0.15, \ldots\}$, positive in solid lines and negative in dashed.

to $U(y) = 1 - y^2$. However, it turned out that weak vortices formed near the upper wall under pressure continuation and grew in strength during wall-speed continuation until the solution gained σ_y symmetry as the wall speed reached zero. In terms of the symmetry groups, the starting plane Couette solution had symmetry group $\langle\sigma_{xy}, \sigma_z, \tau_{xz}\rangle$, continuation to non-zero $\mathrm{d}P/\mathrm{d}x$ broke σ_{xy} symmetry, and σ_y was gained at the final step of wall-speed continuation, resulting in symmetry $\langle\sigma_y, \sigma_z, \tau_{xz}\rangle$. The structure of vortices and streaks in TW1 can roughly be described as two copies of EQ7 stacked on top of each other, with the upper copy either phase-shifted by half a wavelength in x or having $[v, w]$ reversed in sign via mirror symmetry in y. This is apparent from comparison of TW1 in figure 7(*a*) to EQ7 in figure 1(*b*) and EQ7-1 in 3(*b*). The stacking across the midplane is somewhat like the radially opposed structure in the M2 pipe flow solution in figure 3(*a*) of Pringle, Duguet & Kerswell (2009), though TW1 shows mirror symmetry about $y = 0$, whereas M2 is radially antisymmetric.

TW2: Figures 7(*b*) and 8(*c*,*d*) show a spatially periodic travelling-wave solution of channel flow with asymmetry in y and symmetry $\langle\sigma_z, \tau_{xz}\rangle$, obtained from an initial guess from turbulent simulation data (Viswanath 2007; Gibson *et al.* 2009). Specifically, we z-mirror-symmetrized an arbitrary turbulent velocity field of channel flow at $Re = 3750$ in a $2\pi, \pi$ box by applying $\boldsymbol{u} \to (1/2)\,(1 + \sigma_z)\boldsymbol{u}$ and then quenched the turbulent field by lowering the Reynolds number and continuing time integration with the bulk velocity fixed at $2/3$ and the σ_z symmetry enforced by projection

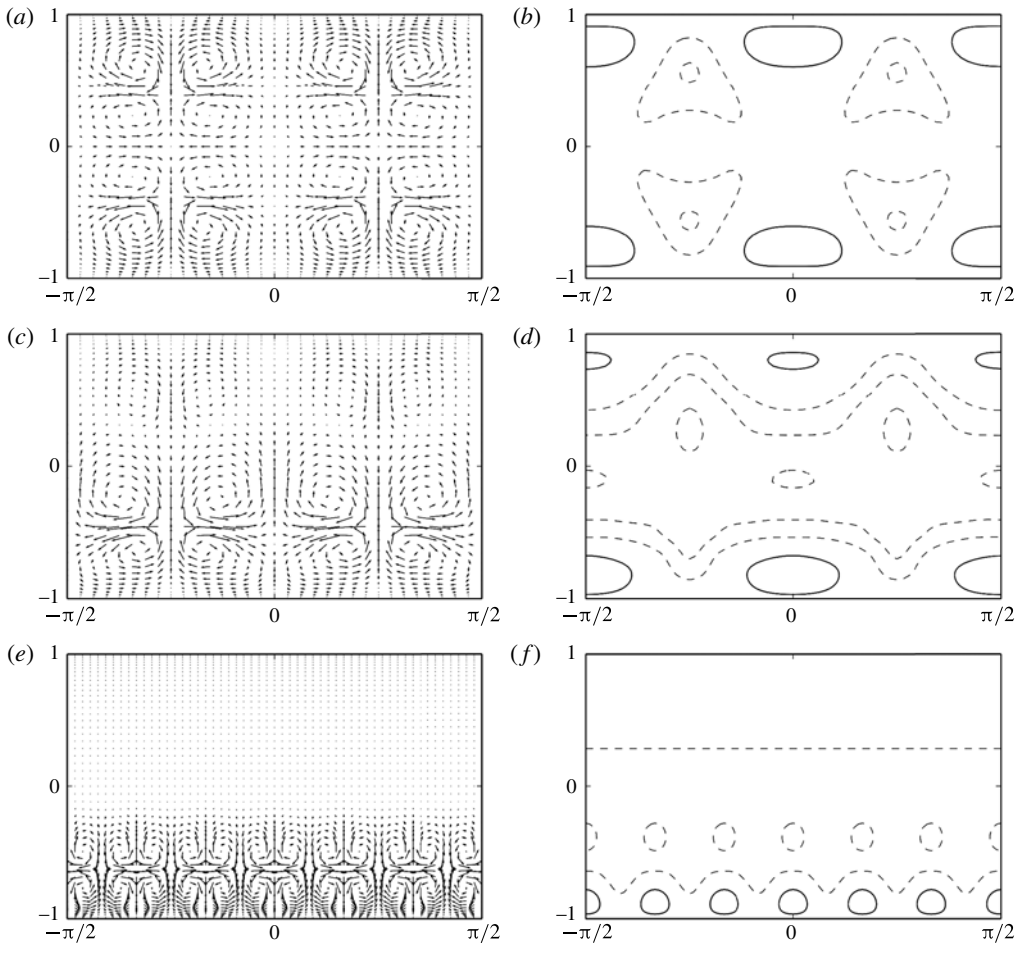

FIGURE 8. Streamwise-averaged roll–streak structure of spanwise-periodic travelling waves of channel flow. Vector plots of x-average $[v, w](y, z)$ and contour plots of x-average $u(y, z)$ for (*a*,*b*) TW1, (*c*,*d*) TW2, and (*e*,*f*) TW3, with the same spatial and Reynolds parameters as in figure 7. Contour lines are shown at levels $u = -0.2, -0.1$ (dashed) and $u = 0.03$ (solid), with an additional negative contour line shown at $u = -0.3$ in (*d*). The vector plots are autoscaled. Axes are z horizontal and y vertical.

at regular intervals. After some experimentation, we found that after quenching to $Re = 2650$, the fine-scale structure of the velocity field and the spatial-mean wall shear decreased quickly, the latter reaching a local minimum after ∼50 time units and growing slowly again for another 50 time units before resuming a high level of wall shear with rapid fluctuations. The smoothness and length of this minimum suggested a close pass to a hyperbolic edge state. Using a velocity field from this minimum as an initial guess for a Newton–Krylov search produced a numerically exact spatially periodic, wall-localized travelling-wave solution of channel flow with $\langle \sigma_z, \tau_{xz} \rangle$ symmetry.

The y asymmetry of TW2 is exaggerated in figure 7(*b*) by the binary character of isosurface plots. In fact at $Re = 2300$ TW2 has weaker vortex structures near the upper wall with swirling strength comparable to those of TW1, and weaker streaks there as

well. Both the vortices and streaks near the upper wall are visible in the streamwise-average plots of TW2 in figure 8(*c*,*d*). Note also that the swirling strength isosurfaces of TW2 in figure 7(*b*) are at $s = \pm 0.10$, over twice the magnitude of those for TW1 in figure 7(*a*) at $s = \pm 0.4$. Compared to the four layers of counter-rotating mean vortices stacked symmetrically about $y = 0$ in TW1 (see figure 8*a*,*b*), TW2 has two layers of counter-rotating mean vortices below $y = 0$ and a single layer of vortices above $y = 0$, and these vortices have the same orientation as the vortices below them. And though it is not clear from the autoscaled vector plots, the mean vortices of TW2 near the lower wall are about three times the magnitude of those of TW1, as measured by magnitudes of the $[v, w]$ velocities, and the mean vortices of TW2 above $y = 0$ are of comparable magnitude to those of TW1. However, the y asymmetry of TW2 increases as the Reynolds number is increased (see TW3) and as z-periodicity is relaxed (see TW2-1 and TW2-2).

TW3: Figures 7(*c*) and 8(*e*,*f*) show a wall-localized, spanwise- and streamwise-periodic travelling wave of channel flow with symmetry $\langle \sigma_z, \tau_{xz} \rangle$, discovered through continuation of TW2 in Reynolds number. The fundamental z wavenumber of TW2 is $\gamma = 2$, but as Re increased towards 4000, the structure at this wavenumber weakened and structure at $\gamma = 6$ grew, while the structure away from the lower wall weakened substantially until it became nearly laminar. TW3 was computed by zeroing all modes in TW2 at $Re = 4000$ with $\gamma < 6$ and refining this initial guess to an exact travelling wave with a Newton–Krylov-hookstep search. The resulting TW3 solution has periodicity $\alpha, \gamma = 1, 6$ and symmetry $\langle \sigma_z, \tau_{xz} \rangle$, where τ_{xz} is understood as involving a half-cell shift in z with respect to the smaller $\ell_z = \pi/3$ periodic length. Its most notable property is its very strong localization in the wall-normal direction, as evidenced by figure 8(*e*,*f*). This is similar to the strong near-wall concentration of the higher-order M-class pipe flow solutions shown in figure 3(*c*,*d*) of Pringle *et al.* (2009).

3.2. *Spanwise-localized travelling-wave solutions of channel flow*

In this section we construct spanwise-localized travelling-wave solutions of channel flow by windowing the spanwise-periodic travelling waves of § 3.1, TW1 and TW2, in different spatial phases. The resulting solutions are illustrated in figures 9–11.

TW1-1: This, shown in figure 9(*a*), was formed by phase-shifting TW1 in z by $\pi/4$ to give it symmetry group $\langle \sigma_y, \sigma_z \tau_x, \tau_{xz} \rangle$, extending this periodic solution from a $2\pi, \pi$ to a $2\pi, 6\pi$ box, windowing the extended periodic solution, and then applying Newton–Krylov-hookstep refinement to the windowed initial guess, producing a spanwise-localized travelling wave with $\langle \sigma_y, \sigma_z \tau_x \rangle$ symmetry. The windowing parameters $a, b = 0.5, 0.4$ were chosen to isolate the central vortex structures in swirling-strength plots. It did not take a great deal of effort to find windowing parameters that gave a successful initial guess; we merely adjusted a and b by tenths until swirling-strength plots of the initial guess appeared similar to the resultant solution in figure 9(*a*). The initial guess for the wave speed was set to the wave speed of the underlying periodic solution TW1, and the pressure gradient was held fixed at $\mathrm{d}P/\mathrm{d}x = -2/Re$ where $Re = 2000$. The Newton–Krylov-hookstep search converged to machine precision in six steps, consuming about half an hour of single-core CPU time on the machine described in § 2.5, for a $24 \times 81 \times 256$ discretization of the $2\pi, 6\pi$ computational domain. The computed solution turned out to be smoother in x and z than the periodic solution on which it was based, enough that $10^{-6} \times 10^{-10} \times 10^{-6}$ truncation levels were retained on a reduced grid of $20 \times 81 \times 192$. Similarly *TW1-2*

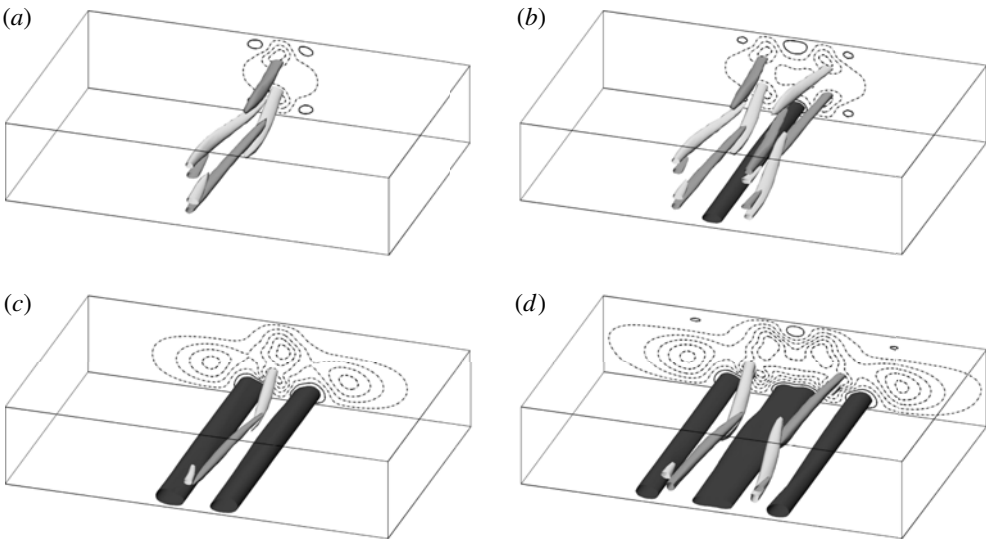

FIGURE 9. Spanwise-localized travelling-wave solutions of channel flow. (*a*) TW1-1, (*b*) TW1-2, (*c*) TW2-1, and (*d*) TW2-2. (*a*,*b*) TW1-1 and TW1-2 are $\langle\sigma_y, \tau_x\sigma_z\rangle$ and $\langle\sigma_y, \sigma_z\rangle$ symmetric travelling waves obtained by localizing TW1 in two different z phases. (*c*,*d*) TW2-1 and TW2-2 are $\tau_x\sigma_z$ and σ_z symmetric travelling waves obtained by localizing TW2 in two different z phases. Plotting conventions are the same as in figure 7, but with isosurfaces of signed swirling strength and streamwise velocity at (*a*,*b*) $s = \pm 0.05$, $u = 0.05$, and (*c*,*d*) $s = \pm 0.10$, $u = 0.08$. Contour lines of streamwise velocity are shown on the back y, z plane at levels $u = 0.03$ (solid lines) and (*a*,*b*) $u = \{-0.03, -0.09, -0.15\}$, (*c*,*d*) $u = \{-0.03, -0.09, -0.15, -0.21, -0.27\}$ (dashed). In (*b*) a high-speed streak near the upper wall, symmetric to that near the lower wall, is suppressed to avoid visual clutter. By contrast, (*c*,*d*) show true asymmetry in high-speed speed streaks: (*c*) has high-speed streaks near the lower wall only, and in (*d*) the streaks near the upper wall are substantially weaker, below the given isosurface levels. Solutions are shown at $Re = 2300$ in $z \in [-3\pi/2,\ 3\pi/2]$ subsets of their full $L_x, L_z = 2\pi, 6\pi$ computational domains.

in figure 9(*b*) was found by refining an initial guess formed from windowing TW1 in its z-phase with $\langle\sigma_y, \sigma_z, \tau_{xz}\rangle$ symmetry and with windowing parameters $a, b = 1.2, 0.4$, resulting in a travelling-wave solution with $\langle\sigma_y, \sigma_z\rangle$ symmetry.

TW2-1 and *TW2-2*, shown in figure 9(*c*,*d*), are probably the most interesting solutions presented in this paper, as they represent travelling-wave solutions that are spanwise localized and strongly concentrated near a single wall and appear similar to important near-wall flow structures identified in previous studies. TW2-1 was formed by windowing TW2 in its z-phase with symmetry $\langle\tau_x\sigma_z, \tau_{xz}\rangle$ and windowing parameters $a, b = 0.6, 0.4$ to get an initial guess with $\tau_x\sigma_z$ symmetry, and refining that with Newton–Krylov-hookstep. We were unable to form TW2-2 by the phase-shifting, windowing, and refining procedure employed for other localized solutions. Instead TW2-2 was formed by shifting TW2-1 leftwards in z until its right-hand high-speed streak was centred on $z = 0$, extending the shifted field from negative to positive z by z-mirror symmetry, and then refining this initial guess with Newton–Krylov-hookstep. We note that TW2-1 and TW2-2 required higher resolution than TW1-1 and TW1-2 to adequately resolve the stronger vortex structure. The computations of TW2-1 and TW2-2 from their initial guesses took about seven CPU hours each.

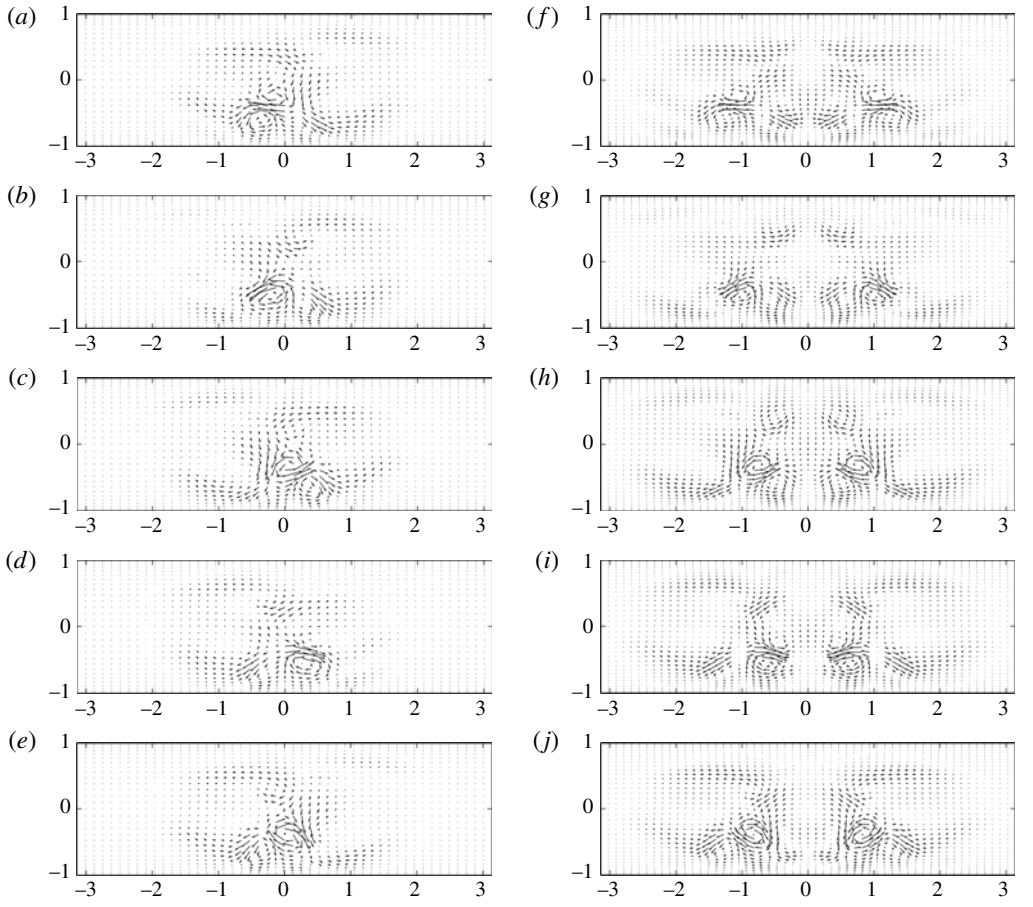

FIGURE 10. Cross-sections of spanwise-localized, near-wall travelling waves of channel flow. (*a–e*) Vector plots of $[v, w](y, z)$ for TW2-1 at $x = \{-\pi, -0.6\pi, -0.2\pi, 0.2\pi, 0.6\pi\}$ and (*f–j*) the same but for TW2-2, with y vertical and z horizontal. Both solutions are at $\alpha = 1$ and $Re = 2300$. The $z \in [-\pi, \pi]$ subset of the full $z \in [-3\pi, 3\pi]$ computational domain is shown.

Each of the travelling-wave solutions depicted in figure 9 is formed from variations of very similar basic structure, which is most clearly seen in isolation in TW2-1 in figure 9(*c*). Near the lower wall there is an x-periodic chain of concentrated vortices, alternating in sign of circulation (clockwise/counter-clockwise), and nearly aligned with the x-axis but tilting slightly in the wall-normal and spanwise directions, as shown in figure 10(*a–e*). The tilting of the chain of alternating vortices results in a non-uniform x-average in the cross-stream flow, specifically, a pair of counter-rotating mean vortices near the wall, figure 11(*a*). The mean vortices draw low-speed fluid upwards between them and high-speed fluid downward on either side, producing the mean high-speed streaks on either side of the mean vortex pair, depicted by solid contour lines in figure 11(*b*). The streamwise momentum exchange induced by the near-wall mean vortices has a net negative effect: the region of mean streamwise flow slower than laminar indicated by negative (dashed) contour lines in figure 11(*b*) is larger in both y, z area and magnitude than the high-speed streaks that outpace

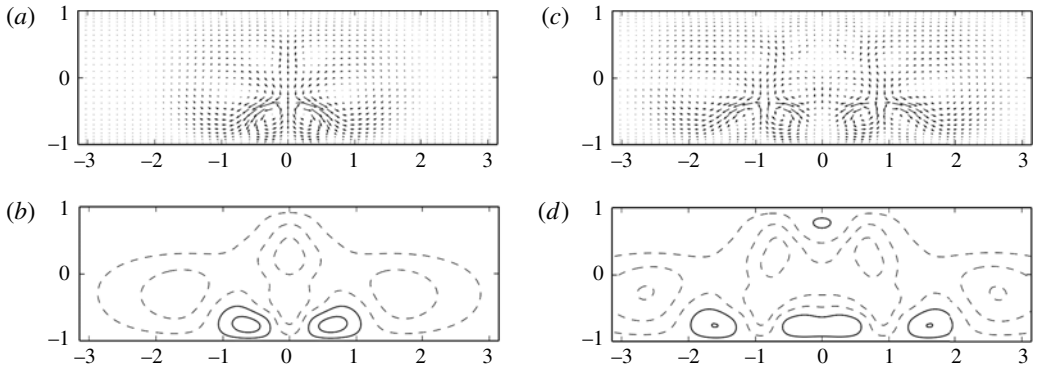

FIGURE 11. Streamwise-averaged roll–streak structure of spanwise-localized travelling waves of channel flow. (*a*) Vector plot of x-average $[v, w]$ and (*b*) contour plot of x-average $u(y, z)$ for TW2-1. (*c*, *d*) The same but for TW2-2. $\alpha = 1, Re = 2300$ for both solutions. Contour lines are plotted at levels $u = \{-0.25, -0.15, -0.05, 0.05, 0.15\}$, with negative values in dashed lines and positive in solid. Vector plots are autoscaled. The $z \in [-\pi, \pi]$ subset of the full $[-3\pi, 3\pi]$ computational domain is shown. Axes are z horizontal and y vertical.

laminar flow, indicated by solid contour lines. Thus the net effect of the roll–streak structure is a decrease of bulk flow relative to laminar for a fixed pressure gradient. TW2-2 roughly consists of two copies of the TW2-1 basic structure, repeated with mirror-symmetry about the $z = 0$ plane. This is evident from comparison of TW2-1 and TW2-2 in figures 9(*c*) and (*d*), 10(*a–e*) and (*f–g*), and 11(*a*,*b*) and (*c*,*d*). TW1-1 and TW1-2 have similar structure to TW2-1 and TW2-2, but with mirror symmetry in y and weaker magnitudes of vorticity (by roughly a factor of two) and integrated velocity deficit relative to laminar (by a factor of four or more).

TW2-1 is very similar to the near-wall coherent structures observed in numerical simulations by Jeong *et al.* (1997) and analysed by Schoppa & Hussain (2002), consisting of alternating, tilted streamwise vortices centred over a sinuous low-speed streak. Jeong *et al.* (1997) produced these structures from conditional samples of numerical simulation data, and Schoppa & Hussain (2002) analysed them as the outcome of non-normal transient growth on a base flow of streamwise-constant, spanwise-varying near-wall streaks. Compare, for example, the tilted alternating vortices of TW2-1 evident in figure 9(*c*) to figure 26 of Schoppa & Hussain (2002). Though these two figures use different visualization schemes (swirling strength versus streamwise vorticity) we have verified that the gross structure is essentially the same with either. The relative orientations of alternating circulation and tilting agree: the light grey vortex in figure 9(*c*) has positive streamwise vorticity and tilts upward in y and towards negative z, as does SP in Schoppa & Hussain (2002); whereas dark grey and SN have negative streamwise vorticity and tilt towards positive z. The tilting angles are roughly comparable: 7° wall-normal and ±8° spanwise tilts for the vortices in TW2-1, compared to 9° and ±4° from Jeong *et al.* (1997). Figure 9(*c*) shows only the high-speed streaks on either side of the alternating vortices; however the low-speed streak beneath the vortices is evident in figure 11(*b*). The low-speed streak of TW2-1 shows sinuous streamwise variation when viewed as a function of x, z (not shown), but the variation in x is weaker than that shown in figure 25 of Schoppa & Hussain (2002). The length scales in wall units match closely: TW2-1

has streamwise-periodic length of 425 wall units, and the tilting vortices extend over ∼60 spanwise units and are confined to $y^+ \leqslant 60$, quite close to the 400 streamwise, 60 spanwise, and $y^+ \leqslant 60$ wall unit lengths evident in figure 6 of Jeong *et al.* (1997).

Exact correspondence between TW2-1 and the cited structures should not be expected, due to differences in their formulation and flow conditions. We conjecture, however, that TW2-1 is formed from the streaky base flow and transient growth mode elements identified by Schoppa & Hussain (2002) in the same way that the NBCW solution of plane Couette flow is formed from the rolls, streaks, and sinuous instability elements of Waleffe's self-sustaining process (Waleffe 2003). Likewise, we suppose that observations of alternating tilted streamwise rolls near the wall in Jeong *et al.* (1997) result from close passes of the flow to the unstable invariant TW2-1 solution, much as the observed roll–streak structures of Hamilton *et al.* (1995) result from close passes to the upper and lower branches of the NBCW solution. TW2-2 bears some degree of resemblance to the lambda vortices that develop as secondary instabilities of Tollmien–Schlichting waves in spatially developing flow. The Λ structure shown in Saiki *et al.* (1993) figure 2(*b*) is evident in TW2-2 in figure 9(*d*), and the cross-stream vector plots of TW2-1 and TW2-2 in figures 10 and 11 resemble the cross-sections of near-wall lambda vortices of developing channel flow shown in Saiki *et al.* (1993) figures 10 and 11. We intend to pursue the connections between TW2-1,2 and previously identified coherent flow structures in future research.

Figure 12 shows a bifurcation diagram for TW1-1,2 and TW2-1,2 under continuation in Reynolds number. The vertical axis of the bifurcation diagram is the integrated velocity deficit, which we define as

$$U_d = -\frac{1}{2L_x}\int_{-L_x/2}^{L_x/2}\int_{-1}^{1}\int_{-L_z/2}^{L_z/2} u(\boldsymbol{x})\,\mathrm{d}x\,\mathrm{d}y\,\mathrm{d}z. \tag{3.1}$$

Since $\boldsymbol{u}(\boldsymbol{x})$ is the perturbation velocity relative to laminar flow at the same Reynolds number and pressure gradient, U_d measures the deficit in streamwise velocity of the travelling wave relative to laminar flow, integrated over the flow domain. As with the integrated shear rate I defined in (2.6), U_d is unnormalized with respect to L_z in order to make it insensitive to the choice of L_z for the z-localized solutions. TW1-1,2 and TW2-2 are each born in saddle–node bifurcations whose upper and lower branches continue smoothly to large Reynolds numbers. The solution curve for TW2-1 is more complex; we were not able to continue it past the point $(Re, U_d) = (1797, 0.395)$. Physical characteristics and discretization parameters of the computed travelling-wave solutions of channel flow are summarized in table 2.

4. Discussion

4.1. *Exponential decay of tails*

The spanwise-localized solutions presented in this paper display a three-part structure: a core region that closely resembles a periodic solution, a transition region, and weak tails that decay to laminar flow. In this section we show that the tails of spanwise-localized streamwise-periodic equilibria are dominated by a mode that decays exponentially at $\mathrm{e}^{-\alpha|z|}$, where α is the fundamental streamwise wavenumber, and that the structure of the tails depends on flow parameters α, Re, the laminar flow profile $U(y)$, and the wave speed c, but not on the details of the solution's core region.

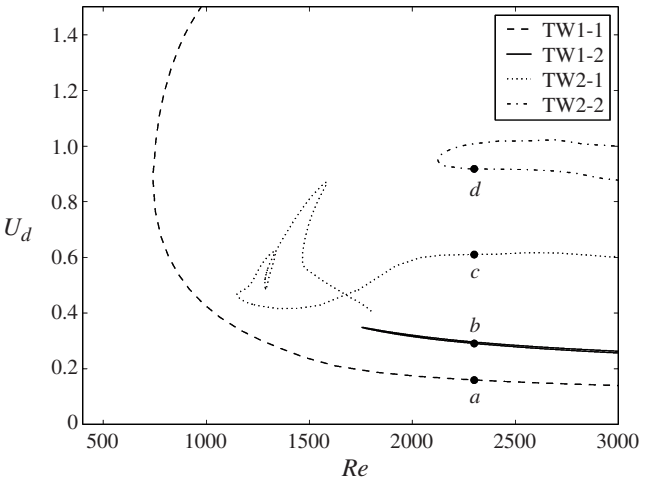

FIGURE 12. Bifurcation diagram of localized solutions of channel flow. Integrated velocity deficit U_d as defined in (3.1) versus Re for localized travelling waves of plane Poiseuille flow. TW1-2 has two distinct branches which appear to overlap at this resolution. Labelled points correspond to solutions in figure 9(*a–d*).

	Symmetry	α, γ	Re	c_x	L_x, L_z	Grid	Accur.	Tails	Pos. λ_r	Max λ_r
TW1	$\langle\sigma_y, \sigma_z, \tau_{xz}\rangle$	1, 2	2300	0.673	$2\pi, \pi$	$24 \times 81 \times 48$	10^{-7}	–	7	0.041
TW1-1	$\langle\sigma_y, \tau_x\sigma_z\rangle$	1, –	2300	0.674	$2\pi, 6\pi$	$20 \times 81 \times 192$	10^{-6}	10^{-5}	6	0.033
TW1-2	$\langle\sigma_y, \sigma_z\rangle$	1, –	2300	0.674	$2\pi, 6\pi$	$20 \times 81 \times 256$	10^{-6}	10^{-5}	8	0.034
TW2	$\langle\sigma_z, \tau_{xz}\rangle$	1, 2	2300	0.564	$2\pi, \pi$	$32 \times 97 \times 64$	10^{-6}	–	29	0.025
TW2-1	$\tau_x\sigma_z$	1, –	2300	0.661	$2\pi, 6\pi$	$24 \times 97 \times 324$	10^{-6}	10^{-5}	17	0.036
TW2-2	σ_z	1, –	2300	0.648	$2\pi, 6\pi$	$24 \times 97 \times 324$	10^{-6}	10^{-5}	36	0.032
TW3	$\langle\sigma_z, \tau_{xz}\rangle$	1, 6	4000	0.475	$2\pi, \pi/3$	$32 \times 109 \times 36$	10^{-7}	–	9	0.035

TABLE 2. Characteristics of localized travelling-wave solutions of channel flow. The streamwise wave speed c_x is in non-dimensionalized units where the centreline velocity of laminar flow is $\bar{U} = 1$. Other quantities are as described in table 1.

As the tails of a spanwise-localized equilibrium or travelling wave approach laminar flow, the perturbation velocity $\boldsymbol{u}$ approaches zero, so we expect $\boldsymbol{u}$ to approximately satisfy the linearized form of (2.1) in which $\boldsymbol{u}\cdot\boldsymbol{\nabla}\boldsymbol{u}$ is set to zero,

$$\frac{\partial \boldsymbol{u}}{\partial t} + U\frac{\partial \boldsymbol{u}}{\partial x} + v\,U'\,\boldsymbol{e}_x = -\boldsymbol{\nabla}p + \frac{1}{Re}\nabla^2\boldsymbol{u}, \quad \boldsymbol{\nabla}\cdot\boldsymbol{u} = 0. \tag{4.1}$$

We look for normal-mode solutions of the form

$$\boldsymbol{u}_{j,\gamma}(\boldsymbol{x}) = \tilde{\boldsymbol{u}}_{j,\gamma}(y)\,\mathrm{e}^{\mathrm{i}(j\alpha(x-ct)+\gamma z)}, \quad p_{j,\gamma}(\boldsymbol{x}) = \tilde{p}_{j,\gamma}(y)\,\mathrm{e}^{\mathrm{i}(j\alpha(x-ct)+\gamma z)} \tag{4.2}$$

where α is real and $\gamma = \gamma_r + \mathrm{i}\gamma_i$ has $\gamma_i > 0$ for tails that decay exponentially as $z \to \infty$. The slowest decaying normal-mode solution, with the smallest positive γ_i, will dominate the tails as $z \to \infty$. For the remainder of this section we drop the j, γ subscripts. To eliminate pressure we convert to velocity–vorticity form by taking the

y-components of the curl and the curl of the curl of (4.1)

$$\left.\begin{aligned}\left(\frac{\partial}{\partial t}+U\frac{\partial}{\partial x}\right)\eta+U'v_z&=\frac{1}{Re}\nabla^2\eta,\\ \left(\frac{\partial}{\partial t}+U\frac{\partial}{\partial x}\right)\nabla^2 v-U''v_x&=\frac{1}{Re}\nabla^4 v,\end{aligned}\right\}\tag{4.3}$$

where $\eta = u_z - w_x$ is the wall-normal vorticity. Boundary conditions are $\eta(x, \pm1, z) = 0$ and $v(x, \pm1, z) = v'(x, \pm1, z) = 0$.

Equation (4.3) and boundary conditions permit a number of types of solution. Where symmetries allow, the solution that dominates behaviour in the tails of localized plane Couette equilibria and travelling waves turns out to be the trivial solution $v = \eta = 0$. This solution in conjunction with the divergence-free condition and the ansatz (4.2) requires that $\tilde{u}_{xx} = -\tilde{u}_{zz}$ and $\tilde{w}_{xx} = -\tilde{w}_{zz}$, which is satisfied by $\gamma = \pm ij\alpha$ and $\tilde{w} = \pm ij\tilde{u}$, the different signs governing exponential decay in the different limits $z \to \pm\infty$. The $j = 1$ mode with $\gamma = \pm i\alpha$ and $\tilde{w} = \pm i\tilde{u}$ thus gives the slowest exponential decay rate ($j = 0$ is ruled out since it does not decay and thus cannot be part of a z-localized solution). The y component of (4.1) gives that $\partial\tilde{p}/\partial y = 0$ so that $\tilde{p}(y) = \tilde{p}$ is a complex constant whose magnitude and phase are set by the pressure conditions at the edge of the transition region at some fixed value of z. The x component of (4.1) gives

$$\tilde{u}'' - i\alpha Re(U - c)\tilde{u} = i\alpha Re\,\tilde{p}.\tag{4.4}$$

The boundary conditions $\tilde{u}(\pm1) = 0$ set the homogeneous solution to zero, so that $\tilde{u}$ and thus $\tilde{w}$ are determined by the fixed value of $\tilde{p}$, the base flow profile $U(y)$, and the parameters α, c and Re. They are independent of the structure of the core-region solution (except for differences of x phase between the $\pm z$ tails resulting from the symmetries of the solution). Thus, the $v = \eta = 0$ solution to the linearized Navier–Stokes equations contributes to the tails an exponentially decaying mode of form $[\tilde{u}(y),\ 0,\ i\tilde{u}(y)]e^{i\alpha(x-ct)-\alpha z}$ as $z \to \infty$.

Figure 13 confirms that over a wide range of α, the tails of EQ7-1 are dominated by u, w components that decay as $e^{-\alpha z}$. Figure 13(a) shows the ∞-norm of u, v and w as a function of z for EQ7-1 at $\alpha = 1$. In this context $\|u\|_\infty(z)$ is the maximum of $|u(x, y, z)|$ over x, y as a function of z. As argued above, the magnitudes of the u and w components are equal in the tails and scale as $e^{-\alpha z}$. The higher-order $e^{-2\alpha z}$ scaling for v results from the quadratic nonlinear term in $u_{1,\gamma}, w_{1,\gamma}$ that has been suppressed on the right-hand side of (4.1) for the $v_{0,\gamma}$ equation for $j = 0$. For figure 13(b), we continued EQ7-1 parametrically in α and observed that the $e^{-\alpha z}$ scaling holds over the explored range of $1/4 \leqslant \alpha \leqslant 2$. For further confirmation of the dominance of $v = \eta = 0$ modes, figure 14(a) compares an x, y slice of streamwise velocity $u(x, y, z)$ from EQ7-1 at a fixed z to figure 14(b), the same as computed from (4.4).

The linearized equations for the tails have solutions other than $v = \eta = 0$; to show that these decay more rapidly than the $v = \eta = 0$ modes (for plane Couette flow), we reduce (4.3) to the eigenvalue equations

$$i\alpha(U - c)\tilde{\eta} + i\gamma U'\tilde{v} = \frac{1}{Re}(\tilde{\eta}'' - (\alpha^2 + \gamma^2)\tilde{\eta}),\tag{4.5}$$

$$i\alpha(U - c)(\tilde{v}'' - (\alpha^2 + \gamma^2)\tilde{v}) - i\alpha U''\tilde{v} = \frac{1}{Re}(\tilde{v}'''' - 2(\alpha^2 + \gamma^2)\tilde{v}'' + (\alpha^2 + \gamma^2)^2\tilde{v}).\tag{4.6}$$

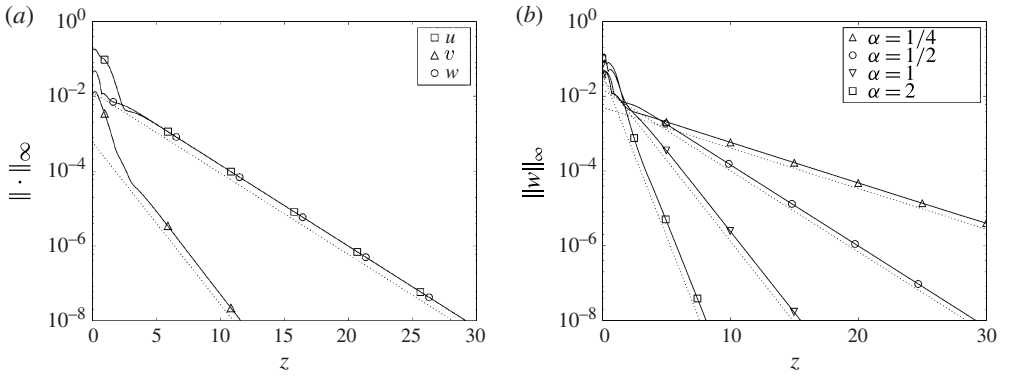

FIGURE 13. Exponential decay in the tails of spanwise-localized plane Couette equilibria. (*a*) Component-wise decay rates for EQ7-1 at $\alpha = 1/2$, $Re = 600$: u, v, w (solid lines) scale as $e^{-\alpha z}, e^{-2\alpha z}, e^{-\alpha z}$ respectively (dotted lines). (*b*) Decay of $\|w\|_\infty$ for EQ7-1 (solid lines) compared to $e^{-\alpha z}$ (dotted lines) at $Re = 600$ and several values of α.

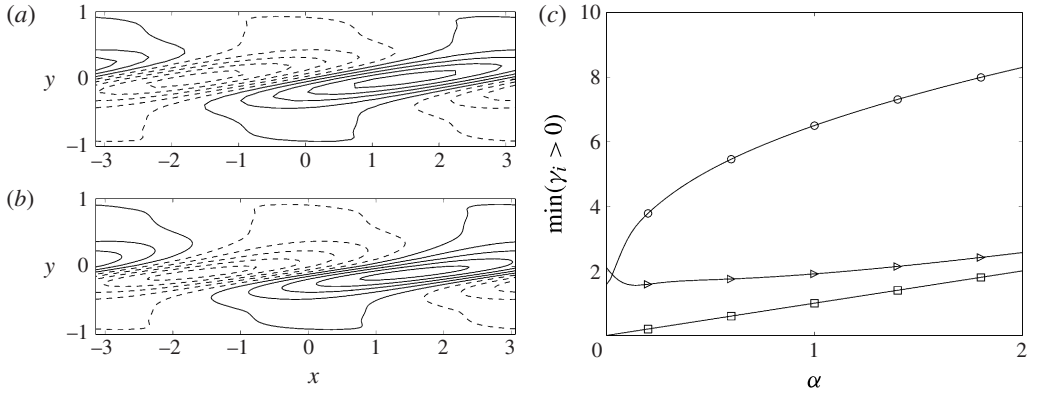

FIGURE 14. (*a*,*b*) Asymptotic form of the tails of spanwise-localized equilibria of plane Couette flow. Contours of streamwise velocity $u(x, y)$ at fixed z: (*a*) a slice of EQ7-1 for $\alpha = 1$ and $Re = 400$, at $z = 11$, where $\|u\|_\infty \approx 10^{-6}$, and (*b*) the asymptotic $v = \eta = 0$ normal-mode solution. Contours are plotted at $\pm[0.15, 0.45, 0.75]$ times the maximum of u, with negative values in dashed lines. (*c*) Exponential decay rate for three types of normal modes in the tails of plane Couette equilibria at $Re = 400$. The minimal γ_i as a function of α is plotted for □, $v = \eta = 0$ solutions; ○, solutions of (4.5) with $\tilde{v}(y) = 0$; and ▷, solutions of (4.6).

The latter is the time-independent form of the familiar Orr–Sommerfeld equation for three-dimensional disturbances. Equation (4.6) is independent of $\tilde{\eta}$ and the eigenvalues γ can be found numerically for given α, c, Re, and $U(y)$. The $i\gamma U'\tilde{v}$ coupling term in (4.5) acts as a non-homogeneous forcing, requiring particular solutions for $\tilde{\eta}(y)$ to match the eigenmodes of (4.6). Eigenvalues distinct from those found for (4.6) can be found by solving (4.5) with $\tilde{v}(y) = 0$. Figure 14(*c*) shows the minimal γ_i allowed by these two equations as a function of α for plane Couette equilibria at $Re = 400$. Note that $v = \eta = 0$ modes have the smallest γ_i for α in the range shown ($\alpha < 2$); thus these modes dominate the behaviour of the tails in all solutions with streamwise wavelength

greater than π. It should be noted, however, that streamwise-constant ($\alpha = 0$) modes can exist in domains of any length L_x, and thus might play a dominant role in short (large α) domains if the symmetries permit them.

4.2. *Asymptotic scaling of streamwise Fourier harmonics*

In this section we provide a numerical account of the large-Reynolds-number behaviour of the periodic and localized solutions developed in previous sections. In particular we measure the scaling of various streamwise Fourier components of the solutions with Re, and we show the development of critical layers at large Re. These features are key to the asymptotic analysis of NBCW suggested by Wang *et al.* (2007) and developed into a complete theory by Hall & Sherwin (2010). The main results are as follows. The streamwise Fourier components of EQ7 and solutions related to it, localized and in channel conditions, obey scaling laws similar to those of NBCW, albeit with different exponents and substantially different magnitudes, suggesting that Hall & Sherwin (2010)'s asymptotic analysis could be carried over to the new solutions. EQ8 and the y-asymmetric channel flow solutions, in contrast, do not fit the asymptotic scaling framework so cleanly. All solutions appear to have well-defined critical layers, however, and the critical layer is particularly simple for EQ7 and its localized counterparts.

As suggested by Wang *et al.* (2007) and developed into a complete theory by Hall & Sherwin (2010), a reduced partial differential equation (PDE) system can be developed for the spatially periodic NBCW solution from an asymptotic analysis of its streamwise Fourier modes and the critical layer that develops at large Reynolds numbers. Wang *et al.* (2007) showed numerically that NBCW has a simplified, quasi-two-dimensional structure in the limit of large Reynolds numbers, with a balance between $O(1)$ streamwise-constant streaks, $O(Re^{-1})$ streamwise-constant rolls, and an $O(Re^{-0.9})$ mode in the first (fundamental) streamwise Fourier harmonic, which concentrates in a critical layer of thickness $O(Re^{-1/3})$. Hall & Sherwin (2010) in turn developed an asymptotic theory for NBCW based on vortex–wave interaction that provides insight into the physics of how these components of NBCW balance, predicts their scaling exponents, and which reduces the computation of the solution from a three-dimensional Navier–Stokes problem at large-Re to a two-dimensional PDE at $Re = 1$ coupled with a linear wave evolution equation. Specifically, the interactions of very small fundamental-mode streamwise waves within the critical layer generate non-zero mean stresses that cause jumps in the pressure and the normal derivative of roll velocity across the critical layer. The jump in roll shear drives the mean rolls, which in turn drive the mean streaks. Hall & Sherwin (2010) show that these effects balance to leading order in Re^{-1}, and that the asymptotic theory also reduces computation of the three-dimensional steady state at high Reynolds number to a simpler two-dimensional calculation at unit Reynolds number coupled with a linear wave evolution equation.

This reduced quasi-two-dimensional PDE model of Hall & Sherwin (2010) is of particular interest to us since a theoretical analysis of spanwise localization in solutions of the Navier–Stokes equations should be easier to develop in the context of a reduced model. There is strong numerical evidence that a theory of localization in solutions of the Navier–Stokes equations might be developed. Schneider *et al.* (2010*b*) noted a remarkable resemblance between the x, y-averaged energy of the localized NBCW solutions and localized solutions of the one-dimensional Swift–Hohenberg equation found by Burke & Knobloch (2007). The similarity was made more

remarkable by Schneider *et al.* (2010*a*)'s demonstration that the localized NBCW solutions undergo homoclinic snaking under continuation in Reynolds number, just as the localized Swift–Hohenberg solutions do under continuations in their bifurcation parameter. For Swift–Hohenberg, homoclinic snaking of localized solutions is quite well understood theoretically via 'spatial dynamics' (Burke & Knobloch 2007). Time independence reduces the fourth-order Swift–Hohenberg PDE for $u(x,\,t)$ to a fourth-order ordinary differential equation (ODE) for $u(x)$, which can then be considered as a four-dimensional dynamical system where x plays the role of time. In this view, spatially periodic solutions correspond to periodic orbits of the spatial dynamics, and spatially localized solutions correspond to homoclinic orbits that start at the origin $u=0$ at $t\to-\infty$, grow away from it along an unstable direction, wander at finite amplitude for some time, and then reapproach $u=0$ at $t\to\infty$ along a stable direction. Localized solutions display approximately periodic form in their core regions when the finite-amplitude excursion away from $u=0$ makes a number of circuits in the neighbourhood of an unstable periodic orbit of the spatial dynamics.

Thus the close correspondence between localized Navier–Stokes solutions and localized Swift–Hohenberg solutions points to the possibility of a theoretical explanation of localization in invariant solutions of the Navier–Stokes equations. It also points to the importance of a reduced PDE system describing the localized solutions, ideally to a one-dimensional system in the spanwise coordinate, to which the idea of spatial dynamics might be applied. We report on the scaling of streamwise Fourier components and the development of a critical layer in the plane Couette and channel solutions because they are essential ingredients for developing such a reduced-order PDE model. We note that Deguchi *et al.* (2013) have in fact extended the asymptotic analysis of Hall & Sherwin (2010) to the case of the spatially periodic EQ7, for large Re and small α, and have identified $\alpha\sim Re^{-1}$ as the distinguished limit at which the reduced-order system breaks down. They also showed that the spanwise-localized EQ7-1 can be produced by a simple continuation of EQ7 in spanwise wavenumber.

The perturbation velocity field of equilibrium and travelling-wave solutions can be expressed as a sum of streamwise (x) Fourier modes in the form

$$\boldsymbol{u}(\boldsymbol{x},\,t)=\sum_j \hat{\boldsymbol{u}}_j(y,\,z)\mathrm{e}^{\mathrm{i}j\theta} \tag{4.7}$$

where $\theta=\alpha(x-ct)$ and where $\hat{\boldsymbol{u}}_{-j}(y,\,z)=\hat{\boldsymbol{u}}_j^*(y,\,z)$ so that $\boldsymbol{u}$ is real-valued. The streamwise-constant mode $\hat{\boldsymbol{u}}_0$ can be decomposed into streamwise streaks $\hat{u}_0(y,\,z)$ and cross-stream rolls $[0,\,\hat{v}_0,\,\hat{w}_0](y,\,z)$. Recall that $\boldsymbol{u}$ is the deviation from laminar flow $U(y)\boldsymbol{e}_x$, with $\boldsymbol{u}_{tot}=\boldsymbol{u}+U(y)\boldsymbol{e}_x$ and $\hat{u}_{tot,0}=\hat{u}_0+U(y)$, so that the streaks are defined relative to laminar flow. Wang *et al.* (2007) define streaks relative to the z-averaged mean flow, but we do not, since z-averaging is inappropriate for spanwise-localized solutions. Hall & Sherwin (2010) refer to the first (fundamental) harmonic $\hat{\boldsymbol{u}}_1(y,\,z)$ or $\hat{\boldsymbol{u}}_1(y,\,z)\exp(\mathrm{i}\alpha(x-ct))+\mathrm{c.c.}$ as the wave mode.

Figure 15 shows the scaling with Reynolds number of the magnitude of the streaks, rolls, waves, and second and third harmonics for a number of plane Couette and channel solutions. The magnitude is computed with the ∞-norm; for example, the magnitude $\|\hat{\boldsymbol{u}}_1\|_\infty$ of the wave is the maximum over $x,\,y,\,z$ and the vector components $[u,\,v,\,w]$ of $\boldsymbol{u}=\hat{\boldsymbol{u}}_1(y,\,z)\mathrm{e}^{\mathrm{i}\alpha x}+\hat{\boldsymbol{u}}_{-1}(y,\,z)\mathrm{e}^{-\mathrm{i}\alpha x}$. A number of these solutions exhibit very clear scaling of the form $\|\hat{\boldsymbol{u}}_j\|_\infty=O(Re^{-\mu_j})$. For example figure 15(*a*) shows that for NBCW, the streaks are $O(1)$, the rolls $O(Re^{-1})$, and the waves $O(Re^{-0.85})$. The streak

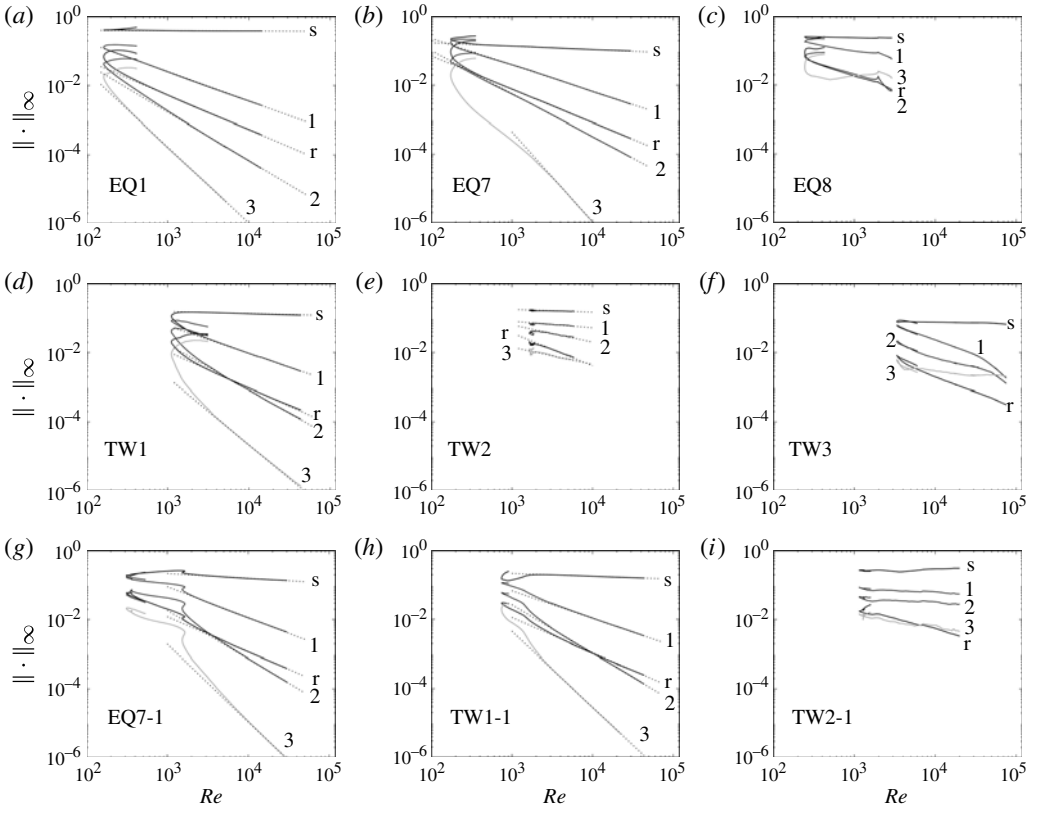

FIGURE 15. Scaling of streamwise Fourier modes of plane Couette and channel solutions. (*a*,*b*,*c*) Spatially periodic plane Couette equilibria NBCW, EQ7, EQ8, at $\alpha, \gamma = 1, 2$. (*d*,*e*,*f*) Spatially periodic channel flow travelling waves TW1, TW2, TW3, at $\alpha, \gamma = 1, 2$. (*g*,*h*,*i*) Spanwise-localized solutions: EQ7-1 plane Couette equilibrium and TW1-1 and TW2-1 channel flow travelling waves, at $\alpha = 1$. The magnitude of various Fourier components of the velocity, as measured by ∞-norm is plotted against Reynolds number (see text). The labels s, r, 1, 2, 3 indicate the streaks $\hat{u}_0$, rolls $[\hat{v}_0, \hat{w}_0]$, and the first, second, and third streamwise Fourier harmonics $\hat{\boldsymbol{u}}_1$, $\hat{\boldsymbol{u}}_2$, and $\hat{\boldsymbol{u}}_3$.

and roll scalings equal the theoretical predictions of Hall & Sherwin (2010), and the wave scaling is within 2 %. Note that the choice of ∞-norm changes the scaling exponent for the NBCW wave component compared to the value of $\mu_1 = 0.9$ reported by Wang *et al.* (2007).

EQ7 in figure 15(*b*) shows equally clear asymptotic scaling with exponents comparable but not equal to those of NBCW. The same is true of all solutions derived from EQ7 by parametric continuation and localization by windowing. Examples of such EQ7-related solutions are shown in figure 15, namely figure 15(*d*) TW1, the spatially periodic travelling wave of channel flow obtained from EQ7 by continuation; figure 15(*g*) EQ7-1, the spanwise-localized equilibrium of plane Couette flow obtained by windowing; and figure 15(*d*) TW1-1, the spanwise-localized travelling wave of channel flow obtained by windowing TW1. Scaling exponents for these solutions plus EQ7-2 and TW1-2 are listed in table 3. It should be noted that the magnitudes of Fourier harmonics of EQ7 and solutions derived from it are substantially different from those of NBCW. For example, comparison of EQ7 in figure 15(*b*) to NBCW in

j		NBCW	EQ7	EQ7-1	EQ7-2	TW1	TW1-1	TW1-2
0	Streak	0.01	0.10	0.14	0.12	0.06	0.08	0.09
1	Wave	0.85	0.77	0.90	0.83	0.80	0.80	0.82
0	Roll	1.00	0.97	1.00	1.00	1.05	1.02	1.00
2		1.40	1.25	1.40	1.35	1.35	1.40	1.35
3		2.20	2.60	2.25	2.45	1.95	2.20	2.00

TABLE 3. Scaling exponents for streamwise Fourier harmonics of equilibrium and travelling-wave solutions of plane Couette and channel flow. Components of solutions $\boldsymbol{u}$ scale as $\|\cdot\|_\infty = O(Re^{-\mu})$ for the given values of μ.

figure 15(*a*) shows that the EQ7 streaks are about a factor of three smaller than those of NBCW, and its fundamental harmonic is about a factor of three larger, resulting in an order of magnitude less scale separation between these components.

In contrast, the upper-branch and y-asymmetric solutions reported here have no clear asymptotic scaling in streamwise Fourier harmonics and substantially poorer separation of scales, namely figure 15(*c*) EQ8, the upper branch of EQ7; figure 15(*e*) TW2, a spanwise-periodic travelling wave of channel flow obtained from judiciously chosen DNS data; figure 15(*f*) TW3, a higher-wavenumber spanwise-periodic travelling wave of channel flow obtained from continuation in Re of TW2; and figure 15(*i*) TW2-1, a spanwise-localized travelling wave of channel flow obtained from windowing TW2. TW2-2 (not shown) is similar to TW2-1. Among these, none of EQ8, TW2, TW2-1, or TW2-2 continue in a straightforward fashion to higher Reynolds number; instead the solutions curves turn around at finite Re and follow complex paths. The same is true for EQ2, the upper branch of NBCW. The numerical evidence thus weighs against the possibility of an asymptotic analysis of these solutions based on streamwise Fourier harmonics.

4.3. *Critical layers*

The development of critical layers is an important consequence of the separation of scales in the streamwise Fourier modes (Wang *et al.* 2007; Hall & Sherwin 2010). The critical layer is the surface on which the mean streamwise fluid velocity matches the wave speed, i.e. $\hat{u}_{tot,0}(y,z) = c$. When higher harmonics become negligible and the roll velocities $\hat{v}_0$, $\hat{w}_0$ are small compared to the streaky streamwise velocity $\hat{u}_{tot,0}$, the equation for the fundamental mode simplifies to

$$\left[\mathrm{i}\alpha(\hat{u}_{tot,0} - c)\hat{\boldsymbol{u}}_1 + (\hat{\boldsymbol{u}}_1 \cdot \boldsymbol{\nabla}\hat{\boldsymbol{u}}_{tot,0})\boldsymbol{e}_x\right] \mathrm{e}^{\mathrm{i}\theta} = \boldsymbol{\nabla}(\hat{p}_1 \mathrm{e}^{\mathrm{i}\theta}) + Re^{-1}\nabla^2(\hat{\boldsymbol{u}}_1 \mathrm{e}^{\mathrm{i}\theta}). \tag{4.8}$$

As argued by Wang *et al.* (2007), for large Re the fundamental harmonic $\hat{\boldsymbol{u}}_1$ concentrates in a region of thickness $\delta = Re^{-1/3}$ about the critical layer, in which (4.8) is dominated by a balance between its first and last terms. For a point $\boldsymbol{x}$ in this region and $\boldsymbol{x}_c$ nearby on the critical layer, this requires a balance of $\alpha(\hat{u}_{tot,0}(\boldsymbol{x}) - c) \approx \alpha(\boldsymbol{x} - \boldsymbol{x}_c) \cdot \boldsymbol{\nabla}\hat{\boldsymbol{u}}_{tot,0}$ against $Re^{-1}\nabla^2$. If $\delta \sim |\boldsymbol{x} - \boldsymbol{x}_c|$ is the thickness of the region, the balance requires $\alpha\delta|\boldsymbol{\nabla}\hat{\boldsymbol{u}}_{tot,0}| \sim Re^{-1}\delta^{-2}$ or $\delta = (\alpha|\boldsymbol{\nabla}\hat{\boldsymbol{u}}_{tot,0}|Re)^{-1/3}$.

Figure 16 illustrates the development of the critical layer for three spatially periodic equilibria of plane Couette flow. For equilibria, the wave speed vanishes, so the critical layer in these plots is the surface $y = f(z)$ on which $u_{tot}(y,z) = 0$. For NBCW, shown in figure 16(*a*,*b*), the height of the critical layer varies in z, and its thickness δ decreases

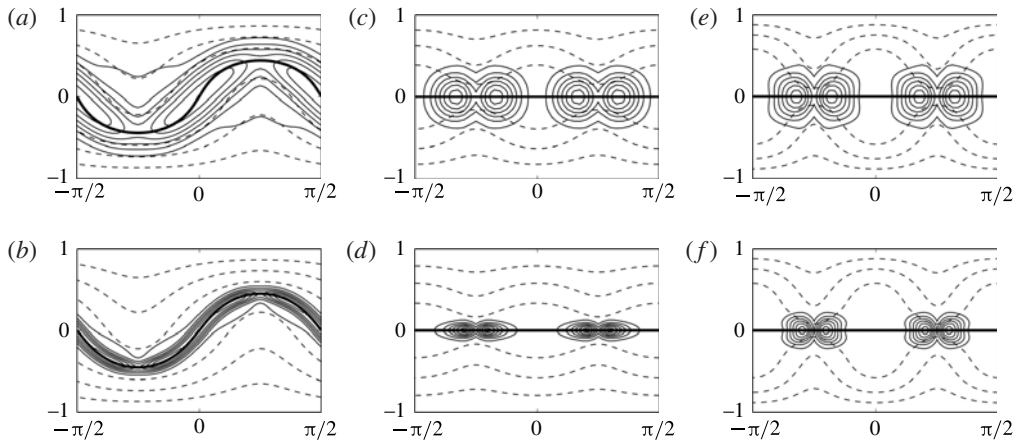

FIGURE 16. Critical layers of spanwise-periodic equilibria of plane Couette flow. (*a*,*b*) NBCW at $Re = 1000$ and 30 000, (*c*,*d*) EQ7 at $Re = 1000$ and 30 000, and (*e*,*f*) EQ8 at $Re = 1000$ and 3000 for streamwise, spanwise wavenumbers $\alpha, \gamma = 1, 2$. Dashed contour lines show total streamwise velocity at levels $u_{tot} = \pm\{0, 0.25, 0.50, 0.75\}$. The critical layer where $u_{tot}(y, z) = c = 0$ is shown with a thick solid contour line. Thin solid contour lines show the autoscaled magnitude of the fundamental Fourier harmonic, $|\hat{\boldsymbol{u}}_1|$. The axes are y vertical and z horizontal.

as $Re^{-1/3}$ between (*a*) $Re = 1000$ and (*b*) $Re = 30\,000$. Figure 16(*a*,*b*) largely duplicates figures 2 and 3 of Wang *et al.* (2007); however we note that our plots show contour lines of $|\hat{\boldsymbol{u}}_1|$ rather than just the vertical component, $|\hat{v}_1|$, and so more clearly convey the fact that, for NBCW, the concentration of the fundamental mode is spread almost uniformly over the entire critical layer.

The critical layers for EQ7 and its upper branch EQ8 are markedly different (figures 16*c*, *d* and 16*e*, *f*). First, the critical layer for these solutions is the line $y = 0$. This follows from their σ_{xy} symmetry, i.e. $[u, v, w](x, y, z) = [-u, -v, w](-x, -y, z)$. Under this symmetry the x-average of the perturbation velocity and total velocity vanishes on $y = 0$. We note that some of the complexity of Hall & Sherwin (2010)'s analysis results from the need to work in a coordinate system aligned with the curved critical layer; for EQ7 and EQ8 this complexity would be eliminated. Second, the fundamental mode $\hat{\boldsymbol{u}}_1$ does not concentrate uniformly over the whole critical layer, but apparently in isolated spots within it. Third, EQ8 seems to form a critical layer at $Re = 2000$, even though its scale separation is much poorer and its large-Re limit does not appear to exist (we were unable to continue it beyond $Re = 3000$).

Figure 17 shows that the critical layer structure of EQ7 carries over directly to its spanwise-localized counterparts EQ7-1 and EQ7-2, with tapering to laminar flow at large $|z|$. In particular the isolated concentrations of $\hat{\boldsymbol{u}}_1$ in the critical layer can be seen, by comparison with figure 5, to result from the first-harmonic x variations of the y, z-localized and concentrated vortex structures. Figure 18(*a*,*b*) shows that the critical layer structure of EQ7 and EQ7-1 carries over to TW1-1, in two copies mirrored symmetrically about $y = 0$. The channel travelling waves have a non-zero wave speed c and lack the σ_{xy} symmetry of EQ7, and therefore have a critical layer $\hat{u}_{tot,0}(y, z) - c = 0$ whose height varies in z.

Figure 18(*c*,*d*) shows critical layer development for the y-asymmetric channel travelling wave TW2-1. Note that y-asymmetry increases while y and z length scales

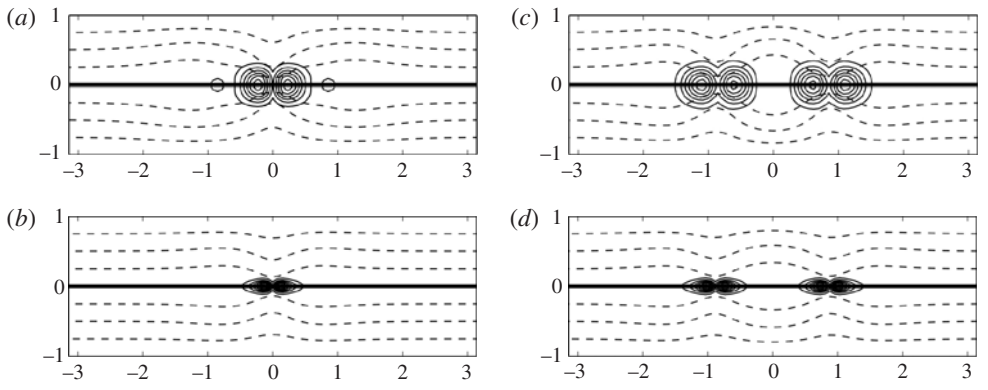

FIGURE 17. Critical layers of spanwise-localized equilibria of plane Couette flow. (*a*,*b*) EQ7-1 at $Re = 1000$ and 30 000 and (*c*,*d*) EQ7-2 at $Re = 1000$ and 30 000 for streamwise wavenumber $\alpha = 1$, with y vertical and z horizontal. Plotting conventions are the same as figure 16. The $z \in [-\pi, \pi]$ subset of the full $[-3\pi, 3\pi]$ computational domain is shown.

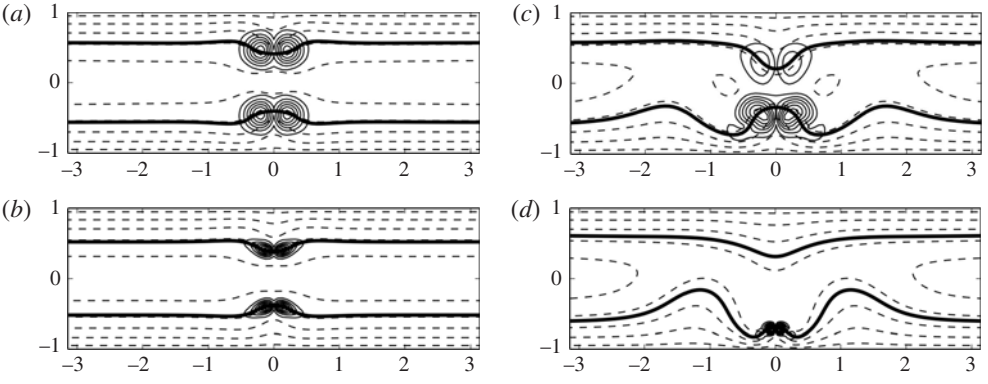

FIGURE 18. Critical layers of spanwise-localized travelling waves of channel flow. (*a*,*b*) TW1-1 at $Re = 2000$ and 30 000 and (*c*,*d*) TW2-1 at $Re = 2000$ and 20 000 for streamwise wavenumber $\alpha = 1$, with y vertical and z horizontal. Plotting conventions are the same as figure 16 except total streamwise velocity contours are shown at levels $u_{tot} = \{0.1, 0.3, \ldots, 0.9\}$. The $z \in [-\pi, \pi]$ subset of the full $[-3\pi, 3\pi]$ computational domain is shown.

decrease with increasing Re. In particular, $\hat{\boldsymbol{u}}_1$ concentrates in a smaller region that approaches the wall as Re increases. An obvious question is whether this represents a near-wall coherent structure that is constant in wall units. We intend to address this question in future work. For the time being we note that the behaviour illustrated in figure 18(*c*,*d*) is still subject to a prescribed length scale in the form of the streamwise wavelength α, and that this prescription must be removed, by streamwise localization or proper scaling with Re, in order for the length scales to be determined naturally.

5. Conclusions

We have found a number of new spanwise-localized equilibrium solutions of plane Couette flow and travelling-wave solutions of channel flow, and additionally a few

spanwise-periodic solutions of channel flow incidental to the construction of the localized solutions. The spanwise-localized solutions consist of a core region that closely resembles a spanwise-periodic solution, a transition region, and exponentially decaying tails. The decay rate of the tails is $e^{-\alpha|z|}$, and their structure is determined solely by the streamwise wavenumber, the laminar flow profile, and the wave speed, and is otherwise independent of the structure of the core region. The solutions related to Itano & Generalis (2009) and Gibson *et al.* (2009)'s HVS/EQ7 display clear scale separation and asymptotic scaling in streamwise Fourier harmonics, suggesting that they are amenable to analysis via a reduced-order PDE retaining only a few harmonics.

Several solutions, namely TW2-1 and TW2-2, capture particularly isolated and elemental exact coherent structures in the near-wall of shear flows, which suggestively resemble structures previously identified in numerical simulations Jeong *et al.* (1997) and analysed in terms of transient growth mechanisms by Schoppa & Hussain (2002). These solutions consist of long bands of concentrated vortices near the walls, with alternating orientation, and roughly aligned with the streamwise axis but tilting slightly in the spanwise and wall-normal directions. The concentrated vortices near the walls are centred over sinuous low-speed streaks and flanked by high-speed streaks very near the walls, and otherwise surrounded by very large regions where the streamwise velocity is reduced relative to the laminar background. These solutions capture, as exact time-independent solutions of the Navier–Stokes equations, the process by which near-wall vortices exchange momentum between the wall and core regions of shear flows and thereby increase drag.

Acknowledgements

The authors thank Tobias Schneider, Greg Chini, Spencer Sherwin, and Philip Hall for illuminating discussions and the referees for valuable suggestions.

REFERENCES

ADRIAN, R. J. 2007 Hairpin vortex organization in wall turbulence. *Phys. Fluids* **19**, 041301.

AUBRY, N., HOLMES, P., LUMLEY, J. L. & STONE, E. 1988 The dynamics of coherent structures in the wall region of turbulent boundary layer. *J. Fluid Mech.* **192**, 115–173.

AVILA, K., MOXEY, D., DE LOZAR, A., AVILA, M. & BARKLEY, D. 2011 The onset of turbulence in pipe flow. *Science* **333** (6039), 192–196.

AVILA, M., MELLIBOVSKY, F., ROLAND, N. & HOF, B. 2013 Streamwise-localized solutions at the onset of turlence in pipe flow. *Phys. Rev. Lett.* **110**, 224502.

BARKLEY, D. & TUCKERMAN, L. S. 2005 Computational study of turbulent laminar patterns in Couette Flow. *Phys. Rev. Lett.* **94**, 014502.

BURKE, J. & KNOBLOCH, E. 2007 Homoclinic snaking: structure and stability. *Chaos* **17** (3), 037102.

CANUTO, C., HUSSAINI, M. Y., QUARTERONI, A. & ZANG, T. A. 2006 *Spectral Methods: Fundamentals in Single Domains*. Springer.

CHANDLER, G. J. & KERSWELL, R. R. 2013 Simple invariant solutions embedded in 2D Kolmogorov turbulence. *J. Fluid Mech.* **722**, 554–595.

CHERUBINI, S., PALMA, P. DE., ROBINET, J.-CH. & BOTTARO, A. 2011 Edge states in a boundary layer. *Phys. Fluids* **23**, 051705.

CLEVER, R. M. & BUSSE, F. H. 1992 Three-dimensional convection in a horizontal layer subjected to constant shear. *J. Fluid Mech.* **234**, 511–527.

CVITANOVIĆ, P. & GIBSON, J. F. 2010 Geometry of turbulence in wall-bounded shear flows: periodic orbits. *Phys. Scr.* T **142**, 014007.

DAVIAUD, F., HEGSETH, J. & BERGE, P. 1992 Subcritical transition to turbulence in plane Couette flow. *Phys. Rev. Lett.* **69**, 2511–2514.

DEGUCHI, K., HALL, P. & WALTON, A. 2013 The emergence of localized vortex-wave interaction states in plane Couette flow. *J. Fluid Mech.* **721**, 58–85.

DENNIS, J. E. & SCHNABEL, R. B. 1996 *Numerical Methods for Unconstrained Optimization and Nonlinear Equations*. SIAM.

DUGUET, Y., PRINGLE, C. C. T. & KERSWELL, R. R. 2008 Relative periodic orbits in transitional pipe flow. *Phys. Fluids* **20**, 114102.

DUGUET, Y., SCHLATTER, P. & HENNINGSON, D. 2009 Localized edge states in plane Couette flow. *Phys. Fluids* **21**, 111701.

FAISST, H. & ECKHARDT, B. 2003 Travelling waves in pipe flow. *Phys. Rev. Lett.* **91**, 224502.

GIBSON, J. F. 2013 Channelflow: a spectral Navier–Stokes simulator in C++. *Tech. Rep.* Univ. New Hampshire, www.channelflow.org.

GIBSON, J. F., HALCROW, J. & CVITANOVIĆ, P. 2008 Visualizing the geometry of state space in plane Couette flow. *J. Fluid Mech.* **611**, 107–130.

GIBSON, J. F., HALCROW, J. & CVITANOVIĆ, P. 2009 Equilibrium and travelling-wave solutions of plane Couette flow. *J. Fluid Mech.* **638**, 1–24.

HALCROW, J., GIBSON, J. F., CVITANOVIĆ, P. & VISWANATH, D. 2009 Heteroclinic connections in plane Couette flow. *J. Fluid Mech.* **621**, 365–376.

HALL, P. & SHERWIN, S. 2010 Streamwise vortices in shear flows: harbingers of transition and the skeleton of coherent structures. *J. Fluid Mech.* **661**, 178–205.

HAMILTON, J. M., KIM, J. & WALEFFE, F. 1995 Regeneration mechanisms of near-wall turbulence structures. *J. Fluid Mech.* **287**, 317–348.

HOF, B., VAN DOORNE, C. W. H., WESTERWEEL, J., NIEUWSTADT, F. T. M., FAISST, H., ECKHARDT, B., WEDIN, H., KERSWELL, R. R. & WALEFFE, F. 2004 Experimental observation of nonlinear travelling waves in turbulent pipe flow. *Science* **305**, 1594–1598.

HOF, B., WESTERWEEL, J., SCHNEIDER, T. M. & ECKHARDT, B. 2006 Finite lifetime of turbulence in shear flows. *Nature* **443** (7107), 59–62.

HOLMES, P., LUMLEY, J. L. & BERKOOZ, G. 1996 *Turbulence, Coherent Structures, Dynamical Systems and Symmetry*. Cambridge University Press.

HOYLE, R. 2006 *Pattern Formation: An Introduction to Methods*. Cambridge University Press.

ITANO, T. & GENERALIS, S. C. 2009 Hairpin vortex solution in planar Couette flow: a tapestry of knotted vortices. *Phys. Rev. Lett.* **102**, 114501.

ITANO, T. & TOH, S. 2001 The dynamics of bursting process in wall turbulence. *J. Phys. Soc. Japan* **70**, 701–714.

JEONG, J., HUSSAIN, F., SCHOPPA, W. & KIM, J. 1997 Coherent structures near the wall in a turbulent channel flow. *J. Fluid Mech.* **332**, 185–214.

JIMÉNEZ, J., KAWAHARA, G., SIMENS, M., NAGATA, M. & SHIBA, M. 2005 Characterization of near-wall turbulence in terms of equilibrium and bursting solutions. *Phys. Fluids* **17**, 015105.

JIMÉNEZ, J. & MOIN, P. 1991 The minimal flow unit in near-wall turbulence. *J. Fluid Mech.* **225**, 213–240.

KAWAHARA, G. 2005 Laminarization of minimal plane Couette flow: going beyond the basin of attraction of turbulence. *Phys. Fluids* **17**, 041702.

KAWAHARA, G. & KIDA, S. 2001 Periodic motion embedded in plane Couette turbulence: regeneration cycle and burst. *J. Fluid Mech.* **449**, 291–300.

KAWAHARA, G., UHLMANN, M. & VAN VEEN, L. 2012 The significance of simple invariant solutions in turbulent flows. *Annu. Rev. Fluid Mech.* **44**, 203–225.

LORENZ, E. N. 1963 Deterministic nonperiodic flow. *J. Atmos. Sci.* **20**, 130.

DE LOZAR, A., MELLIBOVSKY, D., AVILA, M. & HOF, B. 2012 Edge state in pipe flow experiments. *Phys. Rev. Lett.* **108**, 214502.

LUNDBLADH, A. & JOHANSSON, A. V. 1991 Direct simulation of turbulent spots in plane Couette flow. *J. Fluid Mech.* **229**, 499–516.

NAGATA, M. 1990 Three-dimensional finite-amplitude solutions in plane Couette flow: bifurcation from infinity. *J. Fluid Mech.* **217**, 519–527.

NAGATA, M. 1997 Three-dimensional travelling-wave solutions in plane Couette flow. *Phys. Rev.* E **55**, 2023–2025.

OKINO, S., NAGATA, M., WEDIN, H. & BOTTARO, A. 2010 A new nonlinear vortex state in square-duct flow. *J. Fluid Mech.* **657**, 413–429.

PEYRET, R. 2002 *Spectral Methods for Incompressible Flows*. Springer.

PRINGLE, C. T., DUGUET, Y. & KERSWELL, R. R. 2009 Highly symmetric travelling waves in pipe flow. *Phil. Trans. R. Soc.* A **367** (1888), 457–472.

ROBINSON, S. K. 1991 Coherent motions in the turbulent boundary layer. *Annu. Rev. Fluid Mech.* **23**, 601–639.

SAIKI, E. M., BIRINGEN, S., DANABLASOGLU, G. & STREETT, C. L. 1993 Spatial simulation of secondary instability in plane channel flow: comparison of *k*- and *h*-type disturbances. *J. Fluid Mech.* **253**, 485–507.

SCHMIEGEL, A. 1999 Transition to turbulence in linearly stable shear flows. PhD thesis, Philipps-Universität Marburg, available on archiv.ub.uni-marburg.de/diss/z2000/0062.

SCHNEIDER, T. M., GIBSON, J. F. & BURKE, J. 2010*a* Snakes and ladders: Localized solutions of plane Couette flow. *Phys. Rev. Lett.* **104**, 104501.

SCHNEIDER, T. M., GIBSON, J. F., LAGHA, M., LILLO, F. DE & ECKHARDT, B. 2008 Laminar-turbulent boundary in plane Couette flow. *Phys. Rev.* E **78**, 037301.

SCHNEIDER, T. M., MARINC, D. & ECKHARDT, B. 2010*b* Localized edge states nucleate turbulence in extended plane Couette cells. *J. Fluid Mech.* **646**, 441–451.

SCHOPPA, W. & HUSSAIN, F. 2002 Coherent structure generation in near-wall turbulence. *J. Fluid Mech.* **453**, 57–108.

SPALART, P. R., MOSER, R. D. & ROGERS, M. M. 1991 Spectral methods for the Navier–Stokes equations with one infinite and two periodic directions. *J. Comput. Phys.* **96**, 297–324.

STANISLAS, M., PERRET, L. & FOUCAUT, J.-M. 2008 Vortical structures in the turbulent boundary layer: a possible route to a universal representation. *J. Fluid Mech.* **602**, 327–382.

TILLMARK, N. & ALFREDSSON, P. H. 1992 Experiments on transition in plane Couette flow. *J. Fluid Mech.* **235**, 89–102.

UHLMANN, M., KAWAHARA, G. & PINELLI, A. 2010 Travelling-waves consistent with turbulence-driven secondary flow in a square duct. *Phys. Fluids* **22**, 084102.

VAN VEEN, L. & KAWAHARA, G. 2011 Homoclinic tangle on the edge of shear turbulence. *Phys. Rev. Lett.* **107**, 114501.

VISWANATH, D. 2007 Recurrent motions within plane Couette turbulence. *J. Fluid Mech.* **580**, 339–358.

VISWANATH, D. 2009 The critical layer in pipe flow at high Reynolds number. *Phil. Trans. R. Soc. Lond.* A **367**, 561–576.

WALEFFE, F. 1997 On a self-sustaining process in shear flows. *Phys. Fluids* **9**, 883–900.

WALEFFE, F. 1998 Three-dimensional coherent states in plane shear flows. *Phys. Rev. Lett.* **81**, 4140–4143.

WALEFFE, F. 2001 Exact coherent structures in channel flow. *J. Fluid Mech.* **435**, 93–102.

WALEFFE, F. 2003 Homotopy of exact coherent structures in plane shear flows. *Phys. Fluids* **15**, 1517–1534.

WANG, J., GIBSON, J. F. & WALEFFE, F. 2007 Lower branch coherent states in shear flows: transition and control. *Phys. Rev. Lett.* **98** (20), 204501.

WEDIN, H., BOTTARO, A. & NAGATA, M. 2009 Three-dimensional travelling waves in a square duct. *Phys. Rev.* E **79**, 065305.

WEDIN, H. & KERSWELL, R. R. 2004 Exact coherent structures in pipe flow: travelling wave solutions. *J. Fluid Mech.* **508**, 331–371.

WILLIS, A. P., CVITANOVIĆ, P. & AVILA, M. 2013 Revealing the state space of turbulent pipe flow by symmetry reduction. *J. Fluid Mech.* **721**, 514–540.

WU, Y. & CHRISTENSEN, K. T. 2006 Population trends of spanwise vortices in wall turbulence. *J. Fluid Mech.* **568**, 55–76.

ZHOU, J., ADRIAN, R. J., BALACHANDAR, S. & KENDALL, T. M. 1999 Mechanisms for generating coherent packets of hairpin vortices in channel flow. *J. Fluid Mech.* **387**, 353–396.